

# Fully Automated Segmentation and Tracking of the Intima Media Thickness in Ultrasound Video Sequences of the Common Carotid Artery

Dana E. Ilea, Caoimhe Duffy, Liam Kavanagh, Alice Stanton, and Paul F. Whelan, *Senior Member, IEEE*

**Abstract**—The robust identification and measurement of the intima media thickness (IMT) has a high clinical relevance because it represents one of the most precise predictors used in the assessment of potential future cardiovascular events. To facilitate the analysis of arterial wall thickening in serial clinical investigations, in this paper we have developed a novel fully automatic algorithm for the segmentation, measurement, and tracking of the intima media complex (IMC) in B-mode ultrasound video sequences. The proposed algorithm entails a two-stage image analysis process that initially addresses the segmentation of the IMC in the first frame of the ultrasound video sequence using a model-based approach; in the second step, a novel customized tracking procedure is applied to robustly detect the IMC in the subsequent frames. For the video tracking procedure, we introduce a spatially coherent algorithm called adaptive normalized correlation that prevents the tracking process from converging to wrong arterial interfaces. This represents the main contribution of this paper and was developed to deal with inconsistencies in the appearance of the IMC over the cardiac cycle. The quantitative evaluation has been carried out on 40 ultrasound video sequences of the common carotid artery (CCA) by comparing the results returned by the developed algorithm with respect to ground truth data that has been manually annotated by clinical experts. The measured  $IMT_{\text{mean}} \pm \text{standard deviation}$  recorded by the proposed algorithm is  $0.60 \text{ mm} \pm 0.10$ , with a mean coefficient of variation (CV) of 2.05%, whereas the corresponding result obtained for the manually annotated ground truth data is  $0.60 \text{ mm} \pm 0.11$  with a mean CV equal to 5.60%. The numerical results reported in this paper indicate that the proposed algorithm is able to correctly segment and track the IMC in ultrasound CCA video sequences, and we were encouraged by the stability of our technique when applied to data captured under different imaging conditions. Future clinical studies will focus on the evaluation of patients that are affected by advanced cardiovascular conditions such as focal thickening and arterial plaques.

## I. INTRODUCTION

**A**THEROTHROMBOTIC events, myocardial infarction, and stroke are responsible for approximately 35% of the total mortality in the western world and are the lead-

ing causes of morbidity burden world-wide. The first indication of cardiovascular disease is a thickening of the intimal and medial layers of the arterial wall [1], commonly known as intima media thickness (IMT). The intima media complex (IMC) is best visualized in longitudinal sections of the common carotid artery and, as shown in Fig. 1, it is composed of two quasi-parallel lines that represent the lumen intima (LI) and the media adventitia (MA) interfaces. The thickening of the intimal and medial layers is caused by inflammatory-fibroproliferative responses to various forms of insult. It involves lipid accumulation and the migration and proliferation of many cells in the sub-intimal and medial layers, which result in the formation of plaques. It is the rupture of such plaques that causes myocardial infarcts (heart attacks), cerebrovascular events (strokes), peripheral vascular disease (gangrene), and kidney infarcts [2]. To emphasize the impact of the IMC thickening process on the incidence of cardiovascular events, the Rotterdam study indicates that the risk of myocardial infarction increases 43% per standard deviation increase (0.163 mm) in common carotid IMT [3]. The main conclusions resulting from this study were supported by other independent investigations, which reveal that an IMT higher than 0.9 to 1.0 mm indicates a potential atherosclerotic disease [1], [3], [4]. Hence, the robust segmentation and measurement of the IMT has a considerable impact in the early diagnosis of atherosclerosis, prognosis prediction, and in the monitoring of responses to lifestyle and prescribed pharmacological treatments. In addition to the IMT estimation, changes in the mechanical properties of the arterial wall are of interest because they also have the potential to indicate the existence of early cardiovascular diseases. These changes can be detected by analyzing the arterial wall stiffness (or elasticity) using techniques such as diameter change estimation, artery distensibility, or strain imaging [5]–[8].

The current clinical practice in the assessment of the early cardiovascular diseases involves the acquisition of ultrasound data from large superficial arterial vessels such as the common carotid. The image acquisition process generates large ultrasound video sequences that are interpreted using either manual annotation procedures or histologically validated semi-automatic image-processing environments such as the Artery Measurement System (AMS v1.091, Chalmers University, Goteborg, Sweden) [9]–[11].

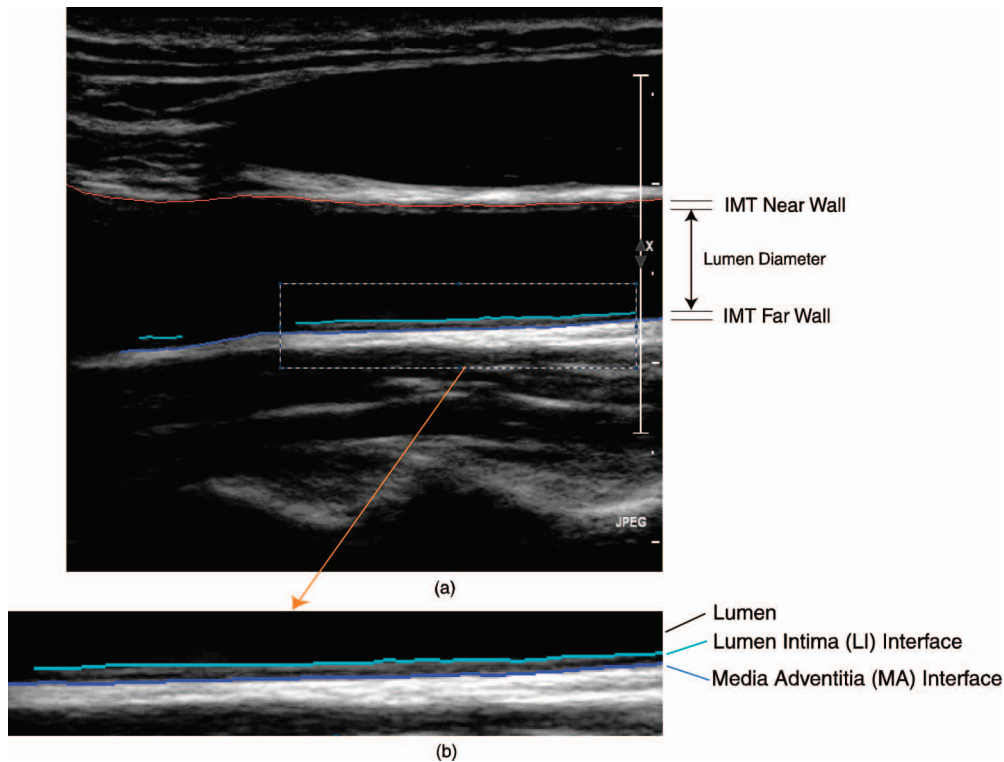



Fig. 1. (a) First frame of a cardiac cycle displaying a longitudinal section of the carotid artery. (b) Detail of the far wall that shows the two anatomical boundaries that compose the intima media complex (IMC), as marked by a medical expert. The intima media thickness (IMT) value is given by the distance between the two interfaces: lumen-intima (LI) and media-adventitia (MA). For this image, we have recorded the following values:  $IMT_{mean} = 0.54$  mm,  $IMT_{min} = 0.4$  mm,  $IMT_{max} = 0.76$  mm, and  $IMT_{median} = 0.5$  mm. 

Although manual assessment generally results in accurate IMT measurements, it is useful to note that the process of annotating multi-frame ultrasound data is not only labor intensive, but is also highly dependent on the experience of the medical practitioner(s). The accuracy of the manual tracing process was analyzed in [12]–[15], and these studies indicate that the results returned by the manual procedures are not reproducible and they are generally characterized by high intra- and inter-user variability [12]–[15]. For instance, the inter-observer consistency of the IMC manual tracing was investigated in [12], where 26 carotid artery images were annotated by 5 clinical experts. The authors conclude that the inter-reader differences are significant and they may affect the correct evaluation of the cardiovascular risk. Prompted by the results reported in [12], the study conducted in [13] indicates that the application of computer-based diagnostic tools has the potential to significantly reduce the inter-user bias. Therefore, the investigation of automatic segmentation techniques can greatly support the clinical practitioners in their evaluation, because they may have substantial benefits in the quality of the medical act, especially in situations in which the developed computer-aided detection (CAD) tools can play the role of the second reader. To address this clinical need, a substantial number of studies were focused on the development of segmentation algorithms that were specifically designed for IMC segmentation in still B-mode ultrasound images. At this stage, it is useful to mention that most of the previous research was concentrated on

the segmentation of the IMC in user-defined frames, and limited research ([16], [17]) was dedicated to the IMT segmentation in video ultrasound sequences. This fact is emphasized in Table I, in which the most representative IMC segmentation techniques are listed. For reasons of completeness, Table I provides a brief technical description for each analyzed IMC segmentation technique, indicates the type of data and the number of patients/data sets used in the clinical study, and gives details in regard to the level of user intervention (these methods will be further analyzed in Section IV, where their accuracy in measuring the IMT will be contrasted to that achieved by the proposed algorithm). In our opinion, the application of single-frame IMC segmentation algorithms in a serial manner to each image of the sequence is problematic because of the lack of inter-frame correlation in video ultrasound data. Indeed, because of the nature of the ultrasound image acquisition process and additional issues induced by motion artifacts, the local contrast between relevant anatomic regions can vary from frame to frame and this may negatively impact on the efficacy of the single-frame IMC segmentation algorithms. To further highlight the limitations associated with single-frame IMC segmentation algorithms, we emphasize two key observations. First, the vast majority of the algorithms that were developed for still (2-D) ultrasound images entail a substantial level of user intervention (for example, 13 of the 18 algorithms described in Table I require user intervention) that would make it impractical to apply them to challenging video CCA data. Second, the

single-frame approach does not allow the development of robust mechanisms that enforce a consistent estimation of the LI and MA interfaces in all frames of the sequence. This fact not only increases the computational time and the error probability associated with the identification of the IMC in CCA video data, but also prevents the coherent localization of the IMT in consecutive frames of the image sequence. These observations identify the fundamental challenges associated with the automatic analysis of the CCA ultrasound video data and they form the major research objective of the work detailed in our paper. The inconsistencies in the appearance of the IMC, which are caused by either patient motion or tissue/arterial deformation during the full cardiac cycle, induce substantial changes in the gradient profiles of the IMC when they are analyzed in a frame-to-frame manner. This issue raises a substantial challenge that must be accommodated by the algorithms that are developed to measure the IMT in CCA video sequences. To adapt to this difficult IMC tracking problem, in this paper a novel unsupervised spatially coherent algorithm called adaptive normalized correlation (ANC) has been introduced. The proposed ANC algorithm has been designed to track the IMC over the cardiac cycle, where piecewise matching constraints were imposed to prevent the algorithm from converging to the wrong arterial interfaces. One important task associated with the IMC tracking procedure is related to the initialization of the LI and MA interfaces in the first frame of the video sequence. This particular issue brings to light the second contribution of this work, which involves the development of an unsupervised IMC segmentation scheme that is able to identify the LI and MA interfaces by fitting a multi-resolution spatially continuous vascular model to the CCA image data. The application of spatial continuity constraints in the process of IMC segmentation proved critical in achieving accurate results and the experimental data demonstrate that the proposed scheme is robust to patient-dependent changes in the morphological structure of the carotid and to variations in ultrasound image quality.

This paper is organized as follows: Section II-A describes the ultrasound video acquisition protocol and provides details about the demographics of the patients involved in our study. Section II-B outlines the computational components of the developed technique; and in Section II-C, the IMC segmentation and tracking algorithms are introduced and presented in detail. Section III presents a comprehensive evaluation of the results obtained by the proposed IMC segmentation and tracking technique and Section IV analyzes the key technical and practical aspects associated with the proposed and state-of-the-art IMC segmentation algorithms. Section V concludes our paper.

## II. MATERIALS AND METHODS

### A. Ultrasound Video Data Acquisition

Our database consists of 40 ultrasound video sequences of longitudinal sections of the CCA that were captured

by our clinical partners from Beaumont Hospital, Dublin, Ireland, from 23 patients. The cohort of patients involved in this study comprised individuals that were free of cardiovascular symptoms at the date of the scan. Seventeen were women with an age range between 21 and 41 years (mean 32 years); the remaining 6 patients were men aged between 30 and 48 years (mean 37 years). This study did not include patients with advanced cardiovascular diseases or plaques; however, several patients presented factors indicating a future risk of cardiovascular events, as follows: 3 patients were current smokers and 4 were ex-smokers, 5 had a family history of heart disease or stroke, 6 patients had cholesterol levels above the recommended limit of 5.0 mmol/L, and 3 of the 17 women included in this analysis had suffered from pre-eclampsia during pregnancy.

Carotid ultrasound examinations of the left common carotid artery were performed using a Phillips iU22 (Phillips Medical Systems, Andover, MA) ultrasound system equipped with L9-3 (with a frequency range of 3 to 9 MHz) and L17-5 (with a frequency range of 5 to 17 MHz) linear-array transducers. Subjects were examined, from a lateral projection, in the supine position with the neck extended and rotated slightly to the contralateral side. B-mode digital cineloop images of the distal common carotid, including approximately 1 cm of the bulb dilatation, were stored on the hard drive of the ultrasound system for off-line analysis. The number of frames per video sequence varies between 37 to 370 (37 frames approximate one full cardiac cycle) and the pixel depth is 8 bits (256 gray levels). The pixel spacing has equal resolutions in the  $x$  and  $y$  directions and ranges between 0.029 to 0.095 mm/pixel; the image size is  $600 \times 800$ . The focus of this work was driven by our clinical partners from Beaumont Hospital, Dublin, who are specifically interested in tracking the IMC for 0.5 s immediately after the R-wave of the electrocardiogram. This allows the quantification of the IMT during both the minimum and the maximum carotid artery distension that correspond to the diastolic and systolic phases, respectively. Depending on the acquisition frequency that is specific for each data set, the number of frames corresponding to the 0.5-s interval ranges between 18 to 29 and the total number of analyzed frames that are evaluated from the 40 ultrasound video sequences is 772. In all 772 frames, both IMC interfaces were manually marked by an ultrasound clinical expert from Beaumont Hospital, Dublin, and all of the annotations were validated by a senior radiologist. An example that illustrates the results of the manual annotation process is shown in Fig. 1.

### B. Outline of the Proposed Algorithm

A complete outline of the proposed IMC segmentation and tracking algorithm is provided in Fig. 2, where the data flow between the constituent modules is illustrated. The algorithm developed to segment the IMC in the first frame of the sequence is completely unsupervised and includes the following computational steps: automatic

TABLE I. OVERVIEW OF STATE-OF-THE-ART IMC SEGMENTATION ALGORITHMS.

Research paper	IMC segmentation method used	Still/ video	# Patients/ sequences	User interaction required
Selzer <i>et al.</i> [16]	Dynamic edge detection segmentation using PROSOUND [18]	Video	24 patients	Yes (initial IMC boundary and manual corrections)
Dwyer <i>et al.</i> [19]	Edge detection using PROSOUND [18]	Still	38 patients	Yes (initial IMC boundary)
Wendelhag <i>et al.</i> [10]	Dynamic programming with cost function minimization	Still	50 patients	Yes (interactive corrections)
Liang <i>et al.</i> [11]	Dynamic programming using a coarse to fine multiscale approach with cost function optimization	Still	50 (CCA)	Yes (cost function weights adjusted using training; corrections)
Liguori <i>et al.</i> [20]	Pattern recognition and edge detection (PRED): - thresholding - gradient intensity profile analysis	Still	30 images	Yes (manual selection of the ROI)
Faita <i>et al.</i> [21]	First-order absolute moment (FOAM) edge detector	Still	42 patients	Yes (manual selection of the ROI)
Golemati <i>et al.</i> [22]	Canny edge detector Hough transform to extract straight lines Selection of dominant lines	Still	10 patients	No (but the method is restricted to strictly horizontal vessels)
Gutierrez <i>et al.</i> [23]	Multiresolution active contours	Still	30 patients	Yes (manual selection of the ROI, manual corrections)
Ilea and Whelan [24]	Spatially continuous vascular model. Proposed steps include: data pre-processing, edge filtering, model selection, edge reconstruction, data refinement.	Still	49 images	No
Destremes <i>et al.</i> [17]	Semi-automatic model-based segmentation based on the estimated distributions from disease free patients. The ROI containing the IMC is modeled using a mixture of three Nakagami distributions.	Video	30 sequences	Yes (initial IMC boundary is constructed using manually inserted points; the mixtures parameters require training)
Loizou <i>et al.</i> [25]	Snakes-based segmentation	Still	100 images	Yes (manual selection of the ROI)
Cheng <i>et al.</i> [26]	Snakes-based segmentation	Still	32 images	Yes (snakes initialization)
Chan <i>et al.</i> [27], 2000	Anisotropic diffusion Active contours segmentation	Still	40 data sets	Yes (manual initialization of the contour)
Rocha <i>et al.</i> [28]	Hybrid dynamic programming-based active contour	Still	47 images, 24 patients	Yes (the user estimates the lumen medial axis with 2 or 3 points)
Delsanto <i>et al.</i> [29]	Snake-based segmentation (snake initialised using gradient-based method)	Still	120 images, 31 patients	No
Molinari <i>et al.</i> [30]	Integrated approach (CALEXia = line fitting followed by fuzzy K-means classification)	Still	200 images	No
Molinari <i>et al.</i> [31]	Multi-resolution edge detection Segmentation using FOAM	Still	365 images	No
Loizou <i>et al.</i> [32]	Snakes-based segmentation [25]	Still	100 images	Yes (see [25])

IMC = intima media complex; CCA = common carotid artery; ROI = region of interest.

region of interest (ROI) detection, multi-resolution edge filtering, IMC model selection, and edge reconstruction. These computational steps are detailed in Section II-C-1.

In the tracking stage of the algorithm, the resulting MA and LI interfaces identified in the first frame are used to initialize the proposed ANC tracking procedure that is applied to identify the IMC interfaces in the subsequent frames of the video ultrasound sequence. Because the MA and LI interfaces show sizeable inter-frame structural inconsistencies (such as variable gaps in the IMC structure) the proposed ANC algorithm has been designed to enforce spatial coherence during the inter-frame tracking process. In the remainder of the paper, each component shown in Fig. 2 will be analyzed in detail.

### C. IMC Video Segmentation

#### 1) IMC Segmentation in the First Frame of the Video Sequence:

a) *Automatic detection of the ROI:* In [24], we introduced a novel approach for ROI detection that proved robust to variations in the local image contrast, type of the ultrasound transducer used for image acquisition, orientation of the transducer relative to the position of the artery, and the size of the artery section that is imaged by the scanner. In this paper, we have further improved this method to enhance its accuracy when applied to low signal-to-noise ratio ultrasound data and additional al-

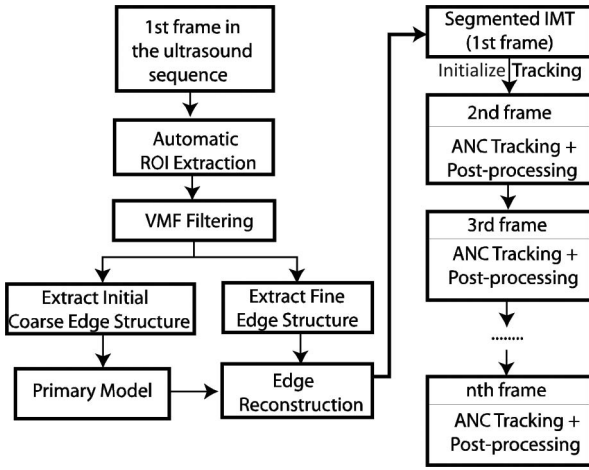


Fig. 2. Outline of the developed intima media complex (IMC) segmentation and tracking algorithm (VMF = vector median filtering; ANC = adaptive normalized correlation).

gorithmic steps were devised to allow its application to image sequences that exhibit unusual arterial morphologies. The main principle behind the proposed approach is to identify the location of the far wall interface [in the remainder of this paper, for purposes of clarity, it will be referred to as the tracked interface (TI)] using a suite of image processing steps that combine the information contained in the intensity domain with knowledge relating to the anatomical structure of the carotid artery. Because the variation of the intensity values in B-mode carotid ultrasound images can be approximated with a bimodal distribution, the proposed algorithm starts with an adaptive thresholding algorithm [33] that is applied to detect the borders between the two main image classes: the blood and the arterial tissues. In this approach, the threshold  $k$  is automatically detected by maximizing the between-

class variance [33]. The thresholding operation results in a binary image where the blood and artery tissue classes are formed:

$$\begin{aligned} \text{if } I(x, y) \leq k &\Rightarrow I(x, y) = 0 \text{ (blood class);} \\ \text{if } I(x, y) > k &\Rightarrow I(x, y) = 255 \text{ (tissue class);} \end{aligned} \quad (1)$$

where  $I(x, y)$  denotes the intensity value of the input image at location  $(x, y)$ . The result after the application of (1) is shown in Fig. 3(b). Next, the thresholded data are subjected to a post-processing refinement step that is applied to eliminate isolated groups of pixels, as follows:

$$\begin{aligned} h^\Gamma(x, y) &= \bigcup_{i=1}^2 b_i = \{b_1, b_2\} \\ b_1 &= \int_\Gamma \delta(I(x, y), 255) d\Gamma, \quad b_2 = \int_\Gamma \delta(I(x, y), 0) d\Gamma \\ \delta(i, j) &= \begin{cases} 1 & i = j \\ 0 & i \neq j. \end{cases} \end{aligned} \quad (2)$$

As illustrated in (2), a histogram  $h^\Gamma(x, y)$  is constructed in a  $\Gamma$  neighborhood around the location  $(x, y)$  in the binary image. An important issue was the identification of the size of the neighborhood  $\Gamma$  that is sufficiently large to ensure statistical relevance for the local distribution  $h^\Gamma(x, y)$ . In our implementation, the size of the neighborhood  $\Gamma$  was set to  $7 \times 7$  around the pixel under analysis,  $b_1$  is the histogram bin that contains the number of white (tissue) pixels and  $b_2$  is the bin generated by the black (blood) image pixels. This distribution will be evaluated to identify the blood pixels that have been incorrectly classed as artery tissues in the result returned from (1). If the value of  $b_1$  is greater than the value of  $b_2$ , then the pixel under analysis has strong local coherence in the intensity domain

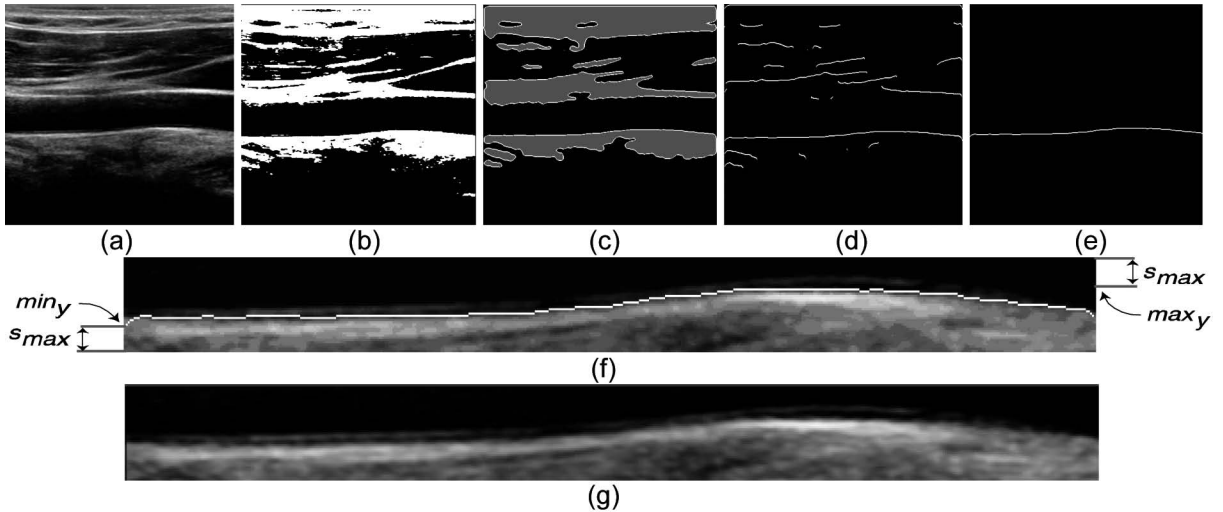


Fig. 3. Automatic region of interest (ROI) detection: (a) Original carotid ultrasound image. (b) Image resulting from the automatic thresholding procedure. (c) The post-processed thresholded data. In this image, the two resulting classes are blood (in black) and the arterial tissue (in gray). The blood-tissue borders are marked in white. (d) The blood-tissue interfaces retained after the application of the test implemented by (3). (e) The automatically detected tracked interface (TI) of the carotid artery. (f) The TI interface superimposed on the ROI, where details about the limits of the ROI are shown. (g) The automatically determined ROI for the image depicted in (a).

and it is classed as a candidate artery tissue pixel (in the output image will be marked with a light gray value). Otherwise (if  $b_2 > b_1$ ), it is assumed that the pixel is generated by noise and is reclassified as a blood pixel (in the output image will be set to 0). The resulting boundary pixels between the two classes after the application of the post-processing step are marked in white in the output image [see Fig. 3(c)], and it can be observed that border pixels are generated not only for the TI interface, but also for other blood-tissue interfaces as well. Then, the next step is to localize the TI interface in this data and the analysis consists of the identification of the blood-tissue interfaces that simultaneously satisfy the following conditions:

- 1)  $I(x, y) = 255$  (border pixel)
- 2)  $I(x, y + \alpha) = 0$  (blood above)
- 3)  $I(x, y - \alpha) > 0$  (tissue below).

The conditions in (3) are applied to Fig. 3(c) as they evaluate the local distribution of the border pixels [ $I(x, y) = 255$ ], and, as indicated earlier, they enforce the anatomic constraint that is characteristic of the TI interface. In this way, the conditions shown in (3) are verified for all blood-tissue interfaces [see the border regions marked in white in Fig. 3(c)] and this process eliminates the blood-tissue interfaces that are not plausible TI candidates [i.e., do not fulfill the three conditions that enforce the requirement to have blood data (black pixels) for  $\alpha$  pixels above the examined blood-tissue interface and artery tissue (light gray pixels) for  $\alpha$  pixels below the interface under examination]. In our implementation, the parameter  $\alpha$  is adaptively detected and in this study the search is carried out in the interval  $[0, 10]$ . The resulting border segments that do not simultaneously satisfy the three conditions in (3) will be filtered out and only a reduced number of segments will be retained for further analysis [see Fig. 3(d)]. To facilitate the accurate identification of the TI, we will enforce additional anatomical constraints that specify that above the TI interface is the lumen area that is always characterized by low-intensity values in the original ultrasound data. Hence, only the segments that have the lowest mean intensity value for  $q$  pixels above the blood-tissue interfaces in Fig. 3(d) will be subjected to further analysis. The parameter  $q$  has been set to a large value (in our implementation,  $q = 50$ ) to allow the accurate identification of the interfaces that are adjacent to the lumen. From the blood-tissue interfaces that were retained from the previous step, we focus our attention on the segment with the largest length because it is the most likely TI candidate. Indeed, following a detailed examination of the B-mode ultrasound images, in the vast majority of cases, the TI is the longest interface from the retained border segments, but our analysis identified less frequent situations in which the blood-tissue interface corresponding to the far wall of the jugular vein generates a border segment that has similar properties relating to the

length and structure of the TI, and sometimes it is slightly larger than the TI interface. Fortunately, the anatomical structure of the carotid data can be again used to elucidate the correct identification of the TI. After the longest border segment from Fig. 3(d) is retained, we will determine whether it belongs to the TI interface by determining whether the second-largest border segment is located at a lumen distance below it. If the second-largest segment is located at the lumen distance, then this second segment is associated with the TI. A complete outline of the operations required to identify the TI interface is presented in a step-by-step manner in Figs. 3(a) to 3(e).

Once the TI is identified using this procedure, the size of the ROI in which the search process for the IMC interfaces will be carried out is selected as follows: the width of the ROI has the same width as the original image and the height is calculated using the expression  $\text{ROI}_{\text{height}} = (\max_y - \min_y) + 2s_{\text{max}}$ , where  $\min_y$  and  $\max_y$  are the minimum and maximum coordinates of the TI on the  $y$  axis, and  $s_{\text{max}}$  is a parameter that allows sampling of sufficient image data above and below the extreme positions of the TI, as illustrated in Fig. 3(f). The parameter  $s_{\text{max}}$  has been experimentally set to 15, because this value ensures the selection of an ROI that includes all image areas where the IMC is present.

*b) IMC segmentation of the first frame in the sequence:*

The speckle pattern is a distinct characteristic of the ultrasound data; it has a random and deterministic nature and is formed by the echoes of coherently distributed sub-resolution scatterers [34]–[38]. The speckle is often perceived as noise because its texture is not directly related to the underlying tissue structure and it degrades the quality of the ultrasound image acquisition process. To attenuate the speckle noise (which has undesirable effects on the extraction of the edge information that is used in the segmentation of the IMC), in the initial stage, the image section sampled by the ROI is filtered using the vector median filtering (VMF) algorithm [39]. The VMF [39] is a nonlinear filtering strategy that excels in the removal of the impulse and multiplicative noise, making it particularly useful for denoising CCA ultrasound data. In addition, the VMF is able to locally smooth the image data while preserving the contextual information, such as edges. The application of the VMF proved to be an important factor in obtaining accurate edge extraction by rejecting the spurious responses caused by the weak textures that are associated with the speckled patterns that are present in the CCA ultrasound data. The concept behind VMF consists of the process of replacing the intensity value of each pixel in the ROI with that of the pixel that is situated in its  $s \times s$  neighborhood that returns the overall minimum Euclidian distance with respect to all pixels that are contained in the  $s \times s$  neighborhood. To prevent edge attenuation that occurs when the filtering procedure is applied for a large window size  $s$ , we applied the VMF filtering in a  $3 \times 3$  neighborhood.

The next step of the IMC segmentation process involves the extraction of the plausible initial coarse edge segments that are associated with the MA and LI interfaces by applying the Canny edge detector [40] to the image data sampled by the ROI. We selected the Canny edge detector because this method is optimal with respect to edge localization and it also avoids issues such as multiple edge responses because it applies a nonmaxima suppression procedure to identify the strongest edge responses in the direction of the gradient. To further improve the selectivity of the edge extraction process, before the calculation of the partial derivatives, the input data are convolved with a Gaussian filter  $G$ ,  $\nabla[I_{\text{ROI}}(x, y) \circ G(x, y, \sigma)]$ , where the scale  $\sigma$  of the Gaussian filter allows a well-controlled and stable edge extraction process. The judicious selection of the scale parameter  $\sigma$  is of particular interest because it opens the possibility of multi-resolution edge extraction. In this regard, if  $\sigma$  is set to high values, only the strong edges that are characterized by significant pixel intensity transitions will be preserved, whereas a small value of  $\sigma$  will result in the extraction of a dense edge structure, where the identification of the coherent image structures would be problematic. This observation motivated us to adopt a coarse-to-fine (or multi-resolution) strategy for the segmentation of the two IMC interfaces. To this end, in the initial stage of the IMC segmentation algorithm, the coarse edge information is extracted with the purpose of detecting the strong IMC edge features that will be further reconstructed using the edge information that is extracted at a finer scale.

*c) Identification of the primary IMC in coarse edge data:*

As previously indicated, the main rationale behind the proposed multi-resolution approach is that the edge information generated at a low scale is too dense to facilitate the robust identification of the IMC. Because the edge segments extracted at a coarse scale are produced by robust salient features that are present in the image, they are used to generate the primary IMC. The primary IMC represents an accurate marker for the identification of the final IMC interfaces that are obtained by completing the coarse edges with the edge data extracted at a finer scale. In the coarse stage of the IMC segmentation process, we set the scale parameter  $\sigma$  to 1.0, a value that ensures that spurious edges that are caused by image noise and weak textures are eliminated. To provide a unique index for each edge segment returned by the Canny edge detector, the coarse edge data are subjected to a labeling procedure.

The primary IMC is constructed by fitting the coarse Canny edges to a spatially continuous vascular model. Because the IMC is defined by a pair of quasi-parallel lines, the plausible IMC segments are only those that are consistent to the slope that is calculated from the detected TI, as it is known that portions from this interface belong to MA. In other words, the parametric representation of the TI provides a geometrical constraint for the two IMC interfaces and its slope will provide us a robust indicator of the orientation of the LI and MA segments. Building on

this concept, we calculate the slope-intercept parameters for all coarse edge segments and only those with slope values close to that calculated for the TI will be retained. The edge segments that do not satisfy the slope criterion will be discarded. In our implementation, the slope-intercept parameters ( $a_p, b_p$ ) of the  $T_p$  edge segment,  $y = a_p x + b_p$ , are estimated using the linear least-square fitting procedure [41]. If  $p$  is the index of the coarse edge segment  $T_p$ , it will be retained for further analysis only if its slope satisfies the condition:  $|a_p - a_{\text{TI}}| < 0.2$ , where  $a_{\text{TI}}$  is the slope of TI. The next operation associated with the construction of the primary IMC interfaces from coarse edge segments involves the enforcement of the echogenicity of the main anatomical structures that are encountered in  $B$ -mode longitudinal ultrasound images of the carotid artery. This implies that the pixels located above the LI interface (lumen area corresponding to blood) will always have lower grayscale values than the pixels situated below the MA interface (which are characterized by high intensity values). This anatomical constraint is always fulfilled and we applied it in the final selection of the coarse edge segments that compose the primary model.

$$A(p) = \left[ \sum_{(x,y) \in [1, n_p]} \sum_{q \in (0,3]} I(x, y + q) \right] / 3n_p \quad (4)$$

$$B(p) = \left[ \sum_{(x,y) \in [1, n_p]} \sum_{q \in (0,3]} I(x, y - q) \right] / 3n_p \quad (5)$$

In (4) and (5),  $p$  is the index of the edge segment under analysis,  $n_p$  is the number of edge pixels associated with the edge segment with index  $p$ ,  $(x, y)$  are the pixel's coordinates,  $A(p)$  is the local mean value of the pixels situated above the segment  $T_p$  and  $B(p)$  is the local mean value of the pixels below the segment  $T_p$ . To obey the anatomic constraints, we propose selection of the MA edge segments for the primary IMC ( $p_{\text{MA}}$ ) if they simultaneously fulfill the two additional conditions

$$\begin{aligned} \text{a) } & A(p_{\text{MA}}) / B(p_{\text{MA}}) < \gamma \\ \text{b) } & B(p_{\text{MA}}) \geq (\max[B(p_{\text{MA}})] - \beta_{\text{ma}}), \end{aligned} \quad (6)$$

where  $p_{\text{MA}}$  are the candidate MA edge segments and  $\beta_{\text{ma}}$  is the parameter that samples the variation in the intensity of the pixels below  $p_{\text{MA}}$ . The  $\gamma$  parameter should be assigned a value smaller than 1.0, because we know that in the case of the MA interface the mean value of the pixels below  $p_{\text{MA}}$  is significantly higher than the mean value of the pixels above it:  $B(p_{\text{MA}}) \gg A(p_{\text{MA}})$ . Experimentally, we set  $\gamma = 0.7$  and this value proved robust in all experiments conducted in our study. This additional test [see the conditions shown in (6)] was applied to eliminate any potential segment that was erroneously labeled as MA during the construction of the MA interface of the primary IMC. A similar procedure has been applied to test the anatomical consistency of the LI edge segments from the primary IMC. An edge segment  $p_{\text{LI}}$  will be classed as belonging to the LI if it has low intensity values in a

$$\text{dist}_{\text{IMT}}(x) = \begin{cases} |y_{\text{MA}}(x) - y_{\text{LI}}(x)|, & \text{if } \text{dist}_{\text{IMT}}(x) \in [\text{dist}_{\text{IMT\_mode}}/2, \text{dist}_{\text{IMT\_mode}} \times 2] \\ 0, & \text{otherwise} \end{cases} \quad (7)$$

region above it when compared with the intensity values of the region beneath it,  $(A(p_{\text{LI}}) / B(p_{\text{LI}})) < \gamma$ . The MA and LI edge segments that fulfill the slope constraint with respect to the TI and the anatomical conditions implemented by (4) through (6) are subjected to a final IMT thickness test. The goal of this test is to identify the spurious edge segments that do not obey the geometric consistency of the IMC model. The thickness analysis is carried out by constructing a distribution (histogram) of the IMT values for all pixels that belong to the primary IMC along the horizontal axis ( $\text{dist}_{\text{IMT}}(x)$  records the distance between the LI and MA segments at position  $x$ ,  $x \in [1, \text{ROI\_width}]$ ), where the probable IMT thickness is calculated as the most frequent value encountered in the histogram,  $\text{dist}_{\text{IMT\_mode}} = \arg \max [\text{hist}(\text{dist}_{\text{IMT}}(x))]$ . This value is denoted as the mode of the IMT thickness histogram ( $\text{hist}(\text{dist}_{\text{IMT}}(x))$ ,  $x \in [1, \text{ROI\_width}]$ ) and is used to check the consistency of all segments that define the primary (coarse) IMC as shown in (7), see above.

The primary IMC obtained for the image shown in Fig. 3(g) is illustrated in Fig. 4(a). At this stage, it is useful to note the improved robustness of the proposed methodology as it enforces a suite of geometrical and anatomic constraints in the identification of the primary IMC, when compared with the unrefined approach based on the search for maxima values in the column intensity profiles that was widely employed by the IMC segmentation techniques that were listed in Table I.

*d) Reconstruction of the coarse IMC using dense edge data:* The last step of the proposed IMC segmentation algorithm involves the completion of the coarse IMC using the edge information that is obtained by applying the Canny edge detector to the VMF filtered data with a lower scale value ( $\sigma = 0.3$ ). In this computational step, the coarse IMC interfaces will be augmented with the fine-scale edge segments that are spatially contiguous and consistent with the geometrical and anatomic constraints that were imposed in the construction of the coarse IMC.

To prevent duplications, the fine-scale edge segments that are situated above and below the primary (coarse) model are eliminated because the IMC interfaces were already determined at those locations.

The remaining fine-scale edge data consist of a large number of edge segments, but only those that are adjacent or positioned in the close vicinity of the coarse primary IMC will be retained for further analysis. To achieve this, a list of edge terminators is extracted for each segment of the primary IMC  $[1, s_{\text{PM}}]$ , where  $s_{\text{PM}}$  defines the number of segments of the primary IMC, and the search for candidate edge segments is initiated in agreement with vicinity and primary IMC geometric constraints. This is achieved by constructing an array in which, for each labeled segment of the primary IMC, the  $x$  and  $y$  coordinates associated with the segment's extreme values (edge terminators) are stored. The search process is applied to identify compatible segments in the fine-scale edge data that are located at the left and right sides of the corresponding edge terminators of the primary IMC. The principle of the search process is shown in Fig. 5, where the left edge terminator of the primary IMC is marked in black. Assuming that the coordinates of the left edge terminators are  $\mathbf{X}_{\text{PM\_L}}$  and  $\mathbf{Y}_{\text{PM\_L}}$ , the search for possible candidate edge points is conducted as shown in Fig. 5. Once a candidate edge pixel that belongs to a fine-scale edge segment is found  $[(X_c, Y_c)]$ , this point acts as a seed point and the neighborhood is iteratively increased to encompass all of the edge points that are connected to it. After the newly detected segments are added to the primary IMC model, the reconstruction process is repeated for the new edge terminators, until all potential IMC segments in the dense edge data are added to the primary IMC.

While the search process shown in Fig. 5 is carried out in large neighborhoods to ensure that all potential fine-scale edge pixels are included in the candidate list, we apply an additional test to determine whether the reconstructed sections that are added to the primary IMC satisfy the conditions depicted in (4) through (6). These

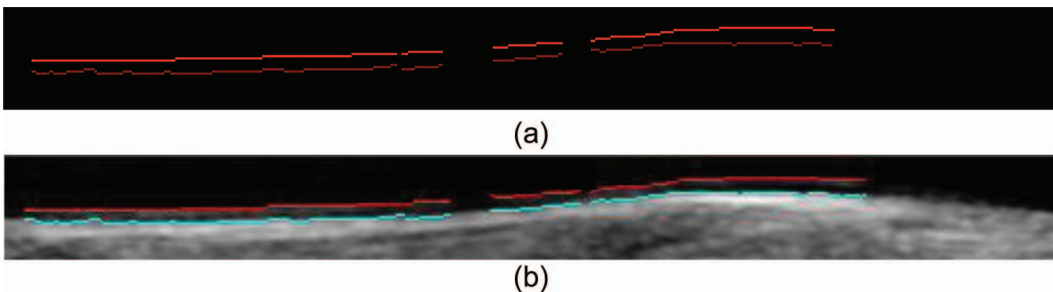



Fig. 4. (a) The primary intima media complex (IMC) model corresponding to Fig. 3(a). (b) The final pair of lines of the IMC resulting after the edge data reconstruction (the mean intima media thickness (IMT) value calculated for this image is 0.48 mm). This diagram is best viewed in color. 



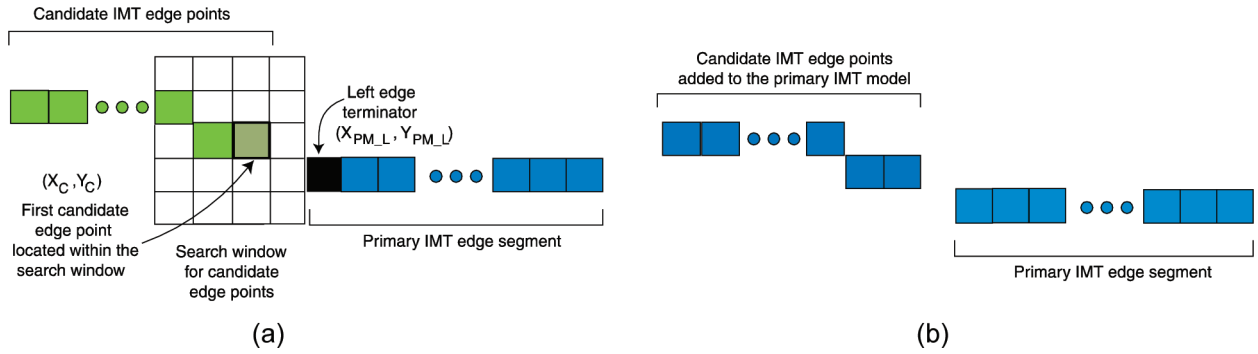



Fig. 5. (a) Example showing the search process employed to identify the dense edge segments situated in the neighborhood of the left edge terminator of the primary intima media complex (IMC). (b) The candidate IMC edge points are added to the primary IMC model. 

conditions are tested to ensure that the reconstructed IMC fine-scale dense edge structure is consistent with the anatomical constraints that were imposed in the selection of the primary IMC. Fig. 4(b) illustrates the final IMC segmentation result for the image shown in Fig. 3(a).

### 2) IMC Tracking in the Subsequent Frames:

During the full cardiac cycle, segments that belong to the two IMC interfaces (LI and MA) are often inconsistent when evaluated on a frame-by-frame basis, because their borders become fuzzy and poorly defined. This situation occurs for both interfaces, but with a higher prevalence for the LI. Although it is theoretically feasible to apply the algorithm detailed in the previous section to each frame, this approach is not desirable for several reasons. The main reason is that the IMC is better defined in the first frames of the cardiac cycle ([16], [17]); another important reason is that the overall motion of the LI and MA interfaces between adjacent frames of the sequence is small. As a result, it is optimal to implement a tracking process that is able to identify the IMC in the subsequent frames of the ultrasound sequence, because the MA and LI interfaces that are identified in the first frame (using the procedure detailed in the previous section) are used for the initialization of the tracking algorithm.

In our initial investigation, we explored the feasibility of applying a strategy based on active contours because these formulations appeared well-suited to serve our track-

ing objectives. Unfortunately, the gradient information that is associated with the MA and LI interfaces shows a significant level of variation in consecutive frames of the video sequence and the results were not as accurate as we initially expected. The most difficult issues were associated with the optimization of the internal parameters and also with the implementation of advection forces that are necessary to prevent the LI interface from settling either on incorrect anatomic structures or on spurious strong gradients that are present in the arterial tissue. To provide a graphical description of these problems, Fig. 6 depicts screenshots detailing the far wall for six consecutive frames, where the inconsistencies in the IMC structure can be observed.

Given the problems encountered when applying active contour-based techniques in the context of IMC tracking, we have developed a different tracking approach. In this paper we introduce a novel tracking strategy called adaptive normalized correlation (ANC) that was specifically designed for the tracking of the IMC over the cardiac cycle. As previously indicated, the inconsistency of the IMC in adjacent frames of the ultrasound sequence is a major challenge in the implementation of robust IMC tracking algorithms, and we believe that this is one of the main reasons that restricted the researchers to evaluation of the IMC in single-frame B-mode ultrasound images (for more details, refer to Table I, where the most relevant IMC segmentation methods are listed). The analysis of

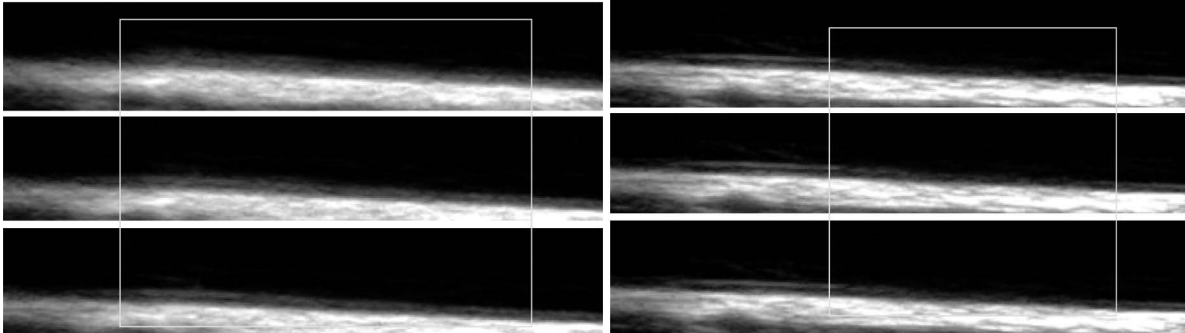


Fig. 6. Screenshots of the far wall for six consecutive frames that detail the changes in the intima media complex (IMC) over a short sequence of the cardiac cycle. In this diagram, the image areas where the IMC shows inconsistencies are highlighted with rectangles.

---


$$\text{ANC}(f_1, f_2, x, y, k) = \sum_{t \in [-\varsigma, \varsigma]} \sum_{(m, n) \in \Omega} \frac{(f_1(x + t + m, y + n) - \overline{f_1(\Omega)})(f_2(x + t + m, y + n + k) - \overline{f_2(\Omega)})}{\sigma_{f_1(\Omega)} \sigma_{f_2(\Omega)}} \quad (8)$$


---

single-frame ultrasound images, as indicated in Section I, provides only a partial answer because they are not able to sample the changes in the IMC over the full cardiac cycle, and as a result they are impractical when applied to serial investigations.

The proposed tracking process is carried out by evaluating the ANC along the  $y$ -axis for all points that define the IMC resulting from the application of the segmentation procedure outlined in Section II-C-1. The main advantage of the proposed ANC-based tracking scheme is that is not hampered by the absence of strong gradients, as is the case with implementations based on active contour strategies. As illustrated in Fig. 6, inconsistencies in the IMC structure often occur during the cardiac cycle, and this will have adverse effects when the pixel-wise tracking process is implemented. To alleviate the problems caused by the gaps in the IMC structure, we have modified the pixel-wise tracking procedure based on normalized correlation (NC) [42] to implement a piecewise-based tracking process. In this regard, the modified NC process is evaluated for each interface for a set of pixels adjacent to the point of interest  $(x, y)$ , as illustrated in (8), see above, and the displacement between the IMC in image  $f_2$  with respect to image  $f_1$  is obtained by maximizing the expression shown in (8):

$$d(x, y) = \arg \max_{k \in [-\omega, \omega]} (\text{ANC}(f_1, f_2, x, y, k)), \quad (9)$$

where  $f_1$  is the current image in the cardiac cycle,  $f_2$  is the next image in the sequence,  $t$  denotes the 1-D neighborhood on the horizontal axis around the pixel of interest with coordinates  $(x, y)$ ,  $\Omega$  is the image neighborhood where ANC is calculated ( $\Omega = 9 \times 9$ ),  $\overline{f_1(\Omega)}$  and  $\overline{f_2(\Omega)}$  are the average intensity values calculated within the neighborhood  $\Omega$  from images  $f_1$  and  $f_2$  at positions  $(x + t, y)$  and  $(x + t, y + k)$ , respectively, and  $k$  defines the interval of variation for the LI and MA interfaces in the vertical direction (along the  $y$ -axis). In our implementation, the parameter  $\varsigma$  has been experimentally determined (optimal results have been obtained for  $t \in [-2, 2]$ ), and for computational reasons the IMC displacement,  $d(x, y)$ , is evaluated in the interval  $k \in [-15, 15]$ , which is larger than any of the IMC displacements that were recorded in the analyzed ultrasound data. As shown in (8), the ANC measure adopts a piecewise data matching approach that is suitable in the presence of weak gradients and missing data estimation by assuming that the movement of a particular weak edge pixel is in agreement with the movement of the  $\varsigma$  left and right neighboring pixels. If a pixel does not have a strong gradient response, we assume that some of the neighbor-

ing pixels do have and the NC values are aggregated along the  $t$  neighborhood, as indicated in (8). The MA and LI interfaces in frame  $f_2$  that correspond to the MA and LI interfaces in frame  $f_1$  are determined using (9), where the displacement is analyzed in the interval  $k \in [-15, 15]$ , i.e.,  $w = 15$ .

The tracking algorithm described in this paper is complemented with a post-processing procedure to improve its accuracy. In the proposed implementation, an additional IMT thickness test is applied to evaluate if there are any outliers or misidentified pixels, by comparing the distances between the MA and LI that are obtained for each pixel position in each frame with the most frequent IMT thickness value that is encountered in the respective frame. If there are isolated pixels that return inconsistent IMT thickness values with respect to the most frequent IMT thickness value, then these pixels are eliminated and image interpolation is applied to bridge the gaps in the IMC.

### III. RESULTS

For the quantitative evaluation of the obtained video segmentation results, a detailed statistical analysis has been conducted (by comparing the results returned by our IMC segmentation and tracking algorithm against the ground truth data that was manually annotated by an experienced clinician from Beaumont Hospital, Dublin). The experimental results that are reported in Section III are obtained using the parameter settings that are indicated in Section II-C.

#### A. Statistical Evaluation of the Video Segmentation Results

To illustrate the performance of the proposed algorithm in a graphical mode, Fig. 7 depicts the IMC segmentation results for the first frames in 12 randomly selected carotid ultrasound sequences. For clarity purposes, the images showed in Fig. 7 display only the ROI that was automatically detected using the algorithm detailed in Section II-C-1.

To quantify the performance of the proposed IMC tracking algorithm, two sets of tests were performed. The first set of tests evaluates the overall border displacement errors for both the LI and MA interfaces detected by the proposed method with respect to the expert's manual annotations. This was achieved by computing the Euclidian distances (or  $L_2$  norm) between the pixels situated on the abscissa of the LI and MA interfaces in the ground truth

data and the corresponding pixels that were identified by the proposed algorithm. To allow for a compact presentation of the experimental results, the calculated errors are reported in Fig. 8 using box plots [28]. Each box plot depicts the minimum and maximum value of the errors, the range between the 25th and the 75th percentile, and the median error value. To complement the experimental results shown in Fig. 8, we also calculated the overall

mean error  $\pm$  standard deviation for the LI ( $LI_{\text{Mean\_Error}} = 0.06 \text{ mm} \pm 0.03$ ) and MA ( $MA_{\text{Mean\_Error}} = 0.08 \text{ mm} \pm 0.04$ ) interfaces. The interquartile range (IQR; i.e., the difference between the 75th and 25th percentile) for the box plot corresponding to the LI interface is 0.03 mm, whereas the calculated IQR for the MA interface is 0.042 mm.

The second set of tests was conducted to calculate statistics related to the mean IMT values that are deter-

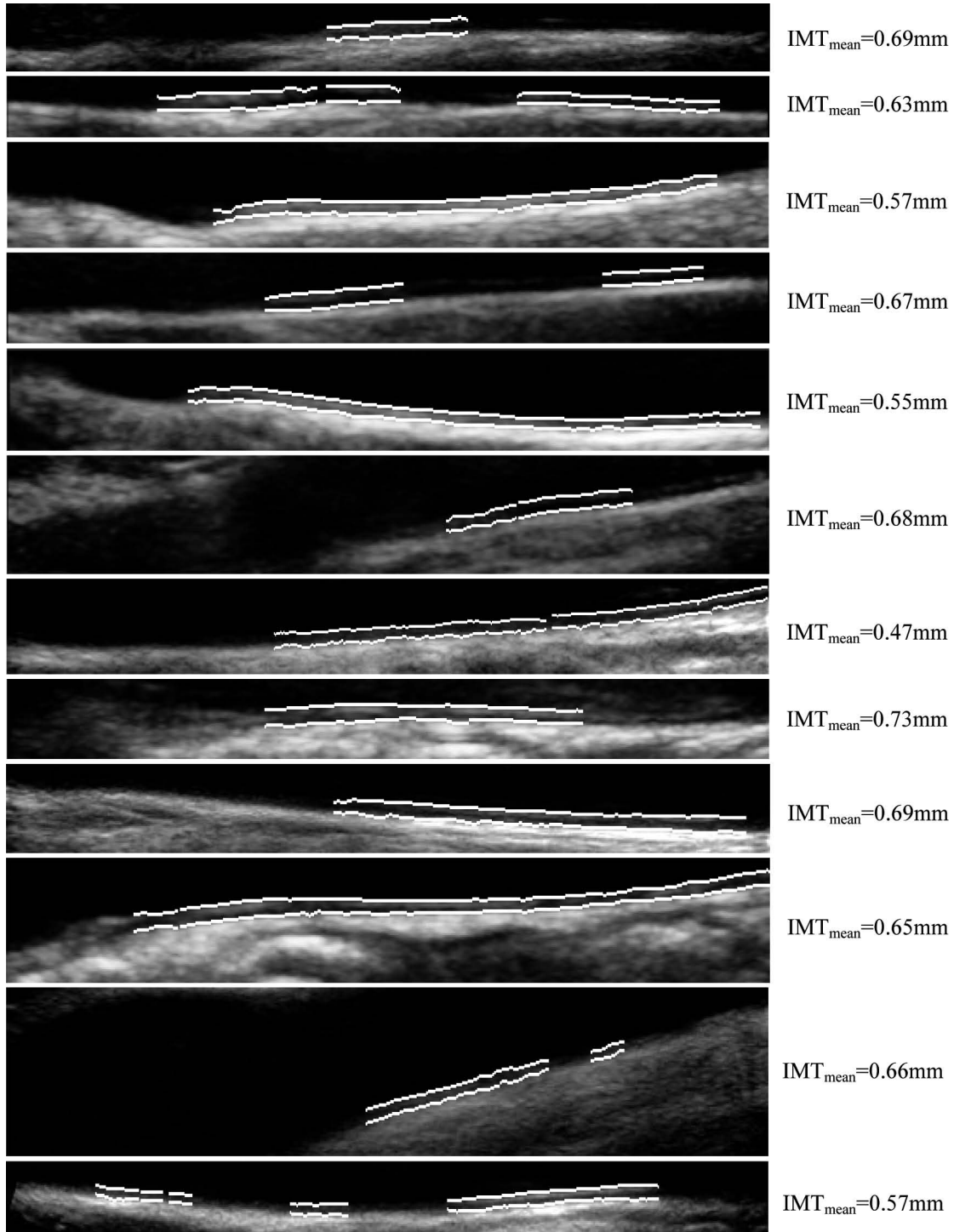


Fig. 7. First frame intima media complex (IMC) segmentation results obtained using the algorithm described in Section II-C-1 for 12 carotid ultrasound sequences. The intima media thickness (IMT) mean value determined by the proposed algorithm is displayed for each corresponding image.

mined by the proposed automatic method and those measured from the manually annotated ground truth data. Fig. 9 depicts the box plots of the mean IMT values calculated for all 40 ultrasound sequences for both automatically segmented (IMT\_Mean\_Seg) and ground truth data (IMT\_Mean\_GT). The overall mean IMT value  $\pm$  standard deviation calculated for the automatically segmented data is 0.60 mm  $\pm$  0.10, whereas the mean IMT value  $\pm$  standard deviation calculated for the ground truth data is 0.60 mm  $\pm$  0.11. As an additional statistical measure, Fig. 9 also reports the IMT mode values which are the most frequent IMT values encountered in each data set in the segmented (IMT\_Mode\_Seg) and in the ground truth (IMT\_Mode\_GT) data. The overall mean  $\pm$  standard deviation values of the IMT mode are 0.59 mm  $\pm$  0.115 and 0.59 mm  $\pm$  0.11 for the automatically segmented and ground truth data, respectively.

Fig. 10 reports additional statistics calculated from the IMT values (IMT<sub>Max</sub>, IMT<sub>Min</sub>, and IMT<sub>Median</sub> values) for both ground truth data and the automatically segmented data.

To evaluate the level of dispersion between the IMT values within the automatically segmented and ground truth data, in Fig. 11 we report the coefficient of variation (CV%) ([10], [25]), which is defined as  $CV\% = (\sigma_{IMT}/\sqrt{2})/IMT_{Mean} \times 100$ . The average value of the CV calculated for all 40 data sets is 2.05% for the automatically segmented data and 5.6% for the ground truth data. The results reported in Fig. 11 indicate a higher variation in the IMT values for ground truth data, which illustrates that the manual annotation process can be easily biased by the subjectivity of the human operator (the problems associated with the manual annotation process are particularly visible in sections of the ultrasound images where the contrast between the MA interface and the surrounding tissue is very low).

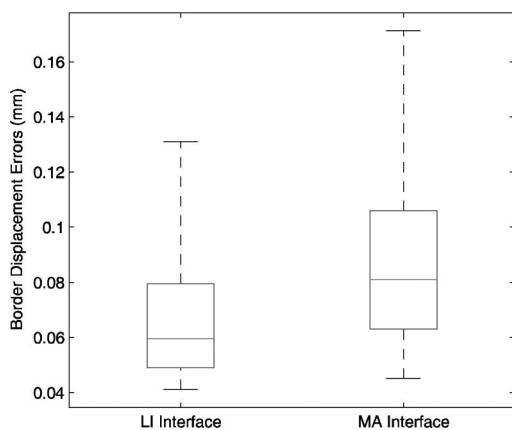


Fig. 8. The overall border displacement errors between the manually segmented lumen intima (LI) and media adventitia (MA) interfaces and the automatically segmented LI and MA interfaces. The overall mean errors are:  $LI_{Mean\_Error} = 0.06$  mm  $\pm$  0.03 and  $MA_{Mean\_Error} = 0.08$  mm  $\pm$  0.04. The calculated interquartile range is:  $IQR_{LI\_Interface} = 0.03$  mm and  $IQR_{MA\_Interface} = 0.042$  mm.

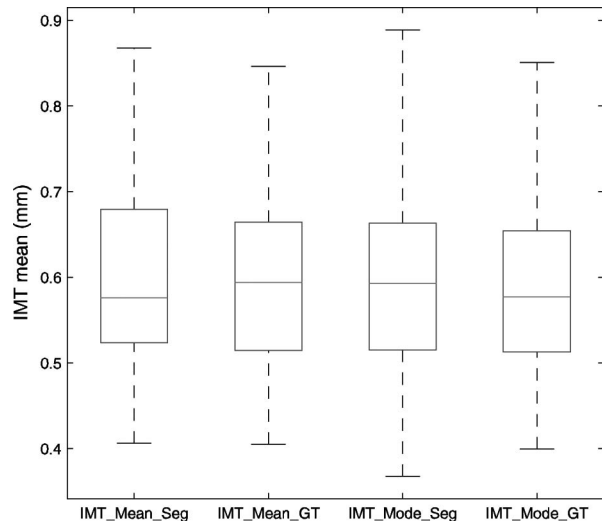


Fig. 9. The mean intima media thickness (IMT) and IMT mode values calculated over the entire database of 40 cardiac sequences for the automatically segmented (Seg) and the ground truth (GT) data. The calculated interquartile range is:  $IQR_{IMT\_Mean\_Seg} = 0.156$  mm,  $IQR_{IMT\_Mean\_GT} = 0.15$  mm,  $IQR_{IMT\_Mode\_Seg} = 0.147$  mm, and  $IQR_{IMT\_Mode\_GT} = 0.141$  mm.

To provide a more detailed measurement that quantifies the performance of the algorithm proposed in this paper, we analyzed the IMT<sub>mean</sub> agreement for all 772 frames between the automatically estimated IMT values with respect to ground truth annotations using Bland–Altman ([43], [44]) and linear regression plots [41].

Fig. 12 illustrates the Bland–Altman plot of the average versus the difference in the mean IMT values between the automatic and manual measurements, where the limits of agreements are  $(-0.007)$  mm  $\pm$  0.176. Fig. 13 depicts the regression plot (the scatter diagram) between the IMT mean values calculated from the ground truth data with respect to the automatically segmented results for all frames of the 40 data sets (772 frames) that were used in our study. As indicated in Fig. 13, the correlation coefficient ( $corr\_coeff$ ) is 0.7, which indicates a good fit between the automatically segmented and manually annotated data. To evaluate the nonparametric significance test between the automatic and manually determined IMT values, we employed the Wilcoxon rank sum test [45] which was calculated for all 772 frames. The calculated

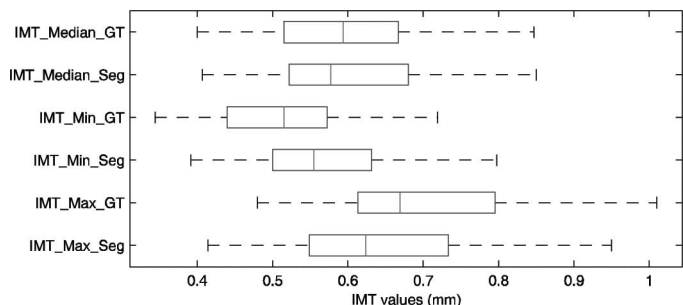


Fig. 10. Additional intima media thickness (IMT) statistics calculated for the 40 ultrasound video data sets used in the experimental study.

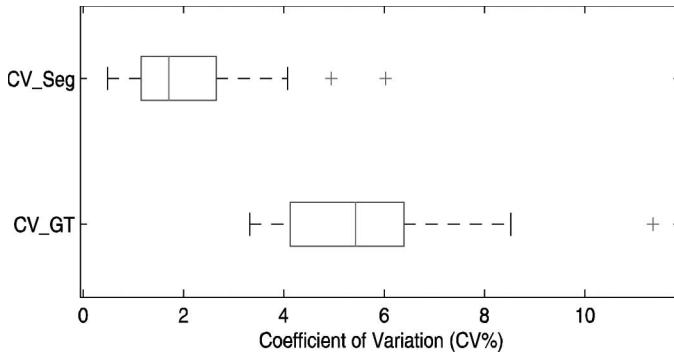


Fig. 11. Box plots of the coefficient of variation (CV%) of the intima media thickness (IMT) mean values calculated for all 40 video sequences for both automatically segmented (CV\_Seg) and ground truth data (CV\_GT).

$p$ -value is 0.25, which indicates a nonsignificant difference between the two sets of measurements (any value of  $p > 0.05$  indicates a nonsignificant difference between the two sets of measurements).

The IMC tracking results also provide information about the dynamic properties of the arterial far wall and examples for four different subjects are illustrated in Fig. 14. Figs. 14(a1) to 14(d1) show the changes in the IMT mean values that are calculated for every frame of the analyzed 0.5 s of the cardiac cycle. In these graphs, the origin (time = 0) corresponds to the end of the diastolic phase of the cardiac cycle, a situation in which the IMT has a maximum value and the arterial diameter reaches its minimal value. During the systolic expansion, the pulse pressure that passes through the carotid causes the compression of the IMC and its decreasing value is illustrated in the plots depicted in Figs. 14(a1) to (d1). The peak systole of the cardiac cycle can be observed in these graphs at the moment where the IMT records the minimal value and the arterial diameter is at its maximum value. These graphs provide additional proof that the proposed algorithm works correctly from end-diastolic to the peak systolic phase of the cardiac cycle, and the IMC deformation patterns depicted in Fig. 14 are in agreement with the clinical studies reported in [16] and [46].

### B. Computational Complexity of the Proposed Method

The computational time required to segment the first frame in the video sequence (using the method in Section II-C-1) is in the range of 6 to 14 s; the time necessary to track the IMC in the subsequent frames covering the 0.5 s of the cardiac cycle ranges from 1.0 to 2.5 s per frame, depending on the length of the LI and MA interfaces. As an example, for the ultrasound sequence (covering the 0.5 s of the cardiac cycle) depicted in Fig. 14(d), the total computational overhead is 31 s (7 s are required to segment the IMC in the first frame and 24 s are required to track the LI and MA interfaces in the subsequent 19 frames). For the 40 video sequences that were used in

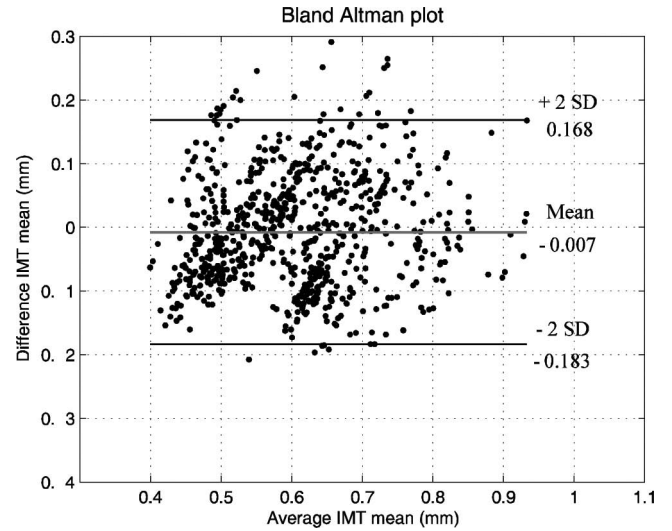


Fig. 12. Bland-Altman plot of the average versus the difference in the intima media thickness (IMT) mean values calculated for all 772 frames contained in the 40 data sets (automatic segmentation with respect to the ground truth data). The middle line represents the mean difference; the upper and lower lines represent the limits of agreement between the two analyzed methods (automatic versus manual), which are defined as the mean  $\pm$  2 standard deviation (SD) of the difference.

our experimental study, the highest overall computational time was attained for the video sequence whose first frame is shown in Fig. 14(b), for which the total segmentation and tracking time was 80 s (8 s to segment the IMC in the first frame and an additional 72 s to track the LI and MA interfaces in the subsequent 28 frames). The computational complexity associated with the IMC segmentation and tracking scheme proposed in this paper is very low when compared with the computational times that

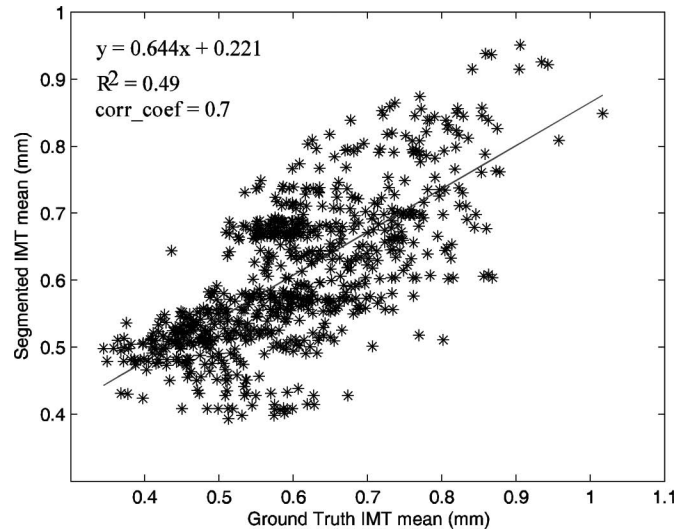


Fig. 13. Regression plot for the mean intima media thickness (IMT) values calculated for all 772 frames representing the 40 data sets contained in the database using the proposed algorithm with respect to the ground truth data. There are three data sets with an IMT value higher than 0.8 mm (which generate 57 stars out of the 772 stars that are plotted for all frames).

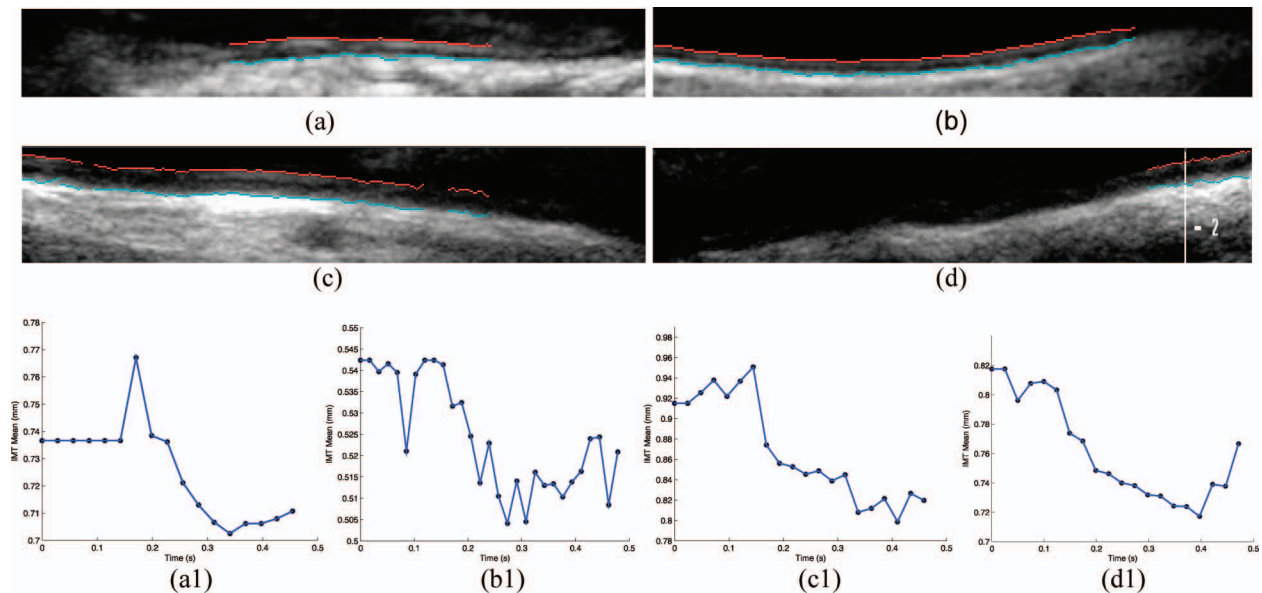


Fig. 14. Dynamic behavior of the  $IMT_{mean}$  during the analyzed 0.5 s of cardiac cycles from four different subjects using the proposed automatic segmentation method. (a), (b), (c), and (d): Regions of interest (ROIs) of the first frames in the cardiac cycles segmented using the method described in Section II-C-1. (a1), (b1), (c1), and (d1): Graphical results illustrating the changes in  $IMT_{mean}$  (calculated for each frame). It can be observed that the  $IMT_{mean}$  values follow a trend; it starts with a slightly higher value at the beginning of the cycle, while during the systolic expansion the intima media thickness (IMT) is compressed, which translates into a decrease in the  $IMT_{mean}$  value. The statistics calculated over the cardiac cycles corresponding to each of these examples are as follows: (a)  $IMT_{Mean} = 0.72$  mm,  $IMT_{Max} = 0.76$  mm,  $IMT_{Min} = 0.70$  mm, and  $IMT_{Median} = 0.73$  mm; (b)  $IMT_{Mean} = 0.52$  mm,  $IMT_{Max} = 0.54$  mm,  $IMT_{Min} = 0.50$  mm, and  $IMT_{Median} = 0.52$  mm; (c)  $IMT_{Mean} = 0.86$  mm,  $IMT_{Max} = 0.95$  mm,  $IMT_{Min} = 0.79$  mm, and  $IMT_{Median} = 0.85$  mm; (d)  $IMT_{Mean} = 0.76$  mm,  $IMT_{Max} = 0.81$  mm,  $IMT_{Min} = 0.71$  mm, and  $IMT_{Median} = 0.74$  mm.

were reported for other published algorithms ([16], [17]; more details are provided in the next section), a fact that further recommends the use of the proposed algorithm in the development of a clinical CAD application. The experiments have been conducted using a 2.4-GHz AMD X2 4600 PC (Advanced Micro Devices Inc., Sunnyvale, CA) running Windows XP (Microsoft Corp., Redmond, WA).

#### IV. DISCUSSION

The experimental data reported in the previous section indicate that the proposed automatic IMC segmentation and tracking technique returns correct results when applied to the identification and measurement of the IMC in ultrasound B-Mode sequences of longitudinal sections of the common carotid artery. Among many issues related to the segmentation and tracking processes, the movement artifacts induced by breathing, inter-patient variation with respect to the structure and mechanical properties of the arterial wall, speckle noise, intra- and inter-frame intensity inconsistencies associated with the LI and MA interfaces that are caused by the non-optimal orientation of the ultrasound probe during image acquisition, and the overall low image contrast proved the most difficult to address during the development of the proposed algorithm. To address these issues, which are common in the analysis of CCA ultrasound data, we have adopted a two-stage unsupervised IMC segmentation and tracking strategy. The first stage deals with the robust identification of the LI

and MA interfaces in the first frame of the video sequence (using a new method that entails the fitting of a multi-resolution spatially continuous vascular model in the analyzed image data), and the second stage involves the application of a novel tracking procedure to track the LI and MA interfaces in the subsequent frames of the CCA ultrasound sequence. The proposed tracking strategy has been specifically designed to accommodate situations in which the LI and MA interfaces exhibit noticeable inconsistencies in the frames that encompass the cardiac cycle.

To allow for a targeted discussion that samples the key aspects related to the analysis of CCA ultrasound image data, in the remainder of this section, we will analyze the most relevant published techniques that addressed this field of research with respect to their performances and the technical aspects associated with the methodology employed to identify/track the IMC in video image data. To emphasize the most apparent advantages associated with the proposed segmentation and tracking scheme, in this discussion, the analysis of the algorithms that were designed to identify the IMC in video (2-D + time) CCA image sequences will be prevalent. This analysis centers on the information collated in Table II, which summarizes the performances obtained by the state-of-the-art IMC segmentation algorithms. Table II provides information regarding the names of the researchers who authored each paper, year of publication, whether the method was developed for the segmentation of still or video ultrasound data, details of the data used in the experimental activity, and performance indicators.

Based on the underlying approach employed by the published works to identify the IMC in CCA ultrasound data, the algorithms in Table II can be broadly categorized as edge-based [16], [18], [19]–[21], [24], [47], [48], active contours [23], [25]–[27], [29], [49], dynamic programming [11], [28], [50], and probabilistic IMC segmentation methods [17]. An initial categorization of the field of research focused on the IMC segmentation has been detailed in [51] and in this section we aim to complement that study by providing an additional analysis of the methods that were developed for the IMC detection/tracking in 2-D + time ultrasound image sequences. As illustrated in Table II, many algorithms have been proposed for the segmentation of still ultrasound frames, and only limited research has been published on the problem of tracking the IMC in video ultrasound sequences. As indicated in the introductory section of this paper, the application of single-frame IMC segmentation in a serial manner, although theoretically feasible, it is impractical because it requires user intervention to accommodate the substantial level of inter-frame variation in imaging conditions, which is a prominent characteristic of the ultrasound image acquisition process. We have conducted a thorough literature search and we were able to find only two papers that explicitly addressed IMC segmentation in video sequences ([16], [17]). In [16], Selzer *et al.* employed an edge detection algorithm to identify the IMC and the vessel diameter over the cardiac cycle. The algorithm detailed in [16] starts with a user-driven annotation procedure in the first frame of the sequence, in which the clinician is required to identify and mark a number of points that belong to the LI and MA interfaces. Next, the authors applied the PROSOUND method [18] to construct the arterial wall interfaces from the manually annotated points. The IMC detected in the first frame is used as input for the PROSOUND method that was also applied to identify the LI and MA interfaces in the subsequent frames of the sequence. During the tracking process, the user is required to correct the errors that may occur in the identification of the IMC (the authors indicated that most errors occur during the systolic expansion and are caused by problems related to the errors in the initialization of the PROSOUND algorithm). The minimum and maximum IMT values were recorded for 24 CCA video sequences and the results reported by the authors are provided in Table II.

A more recent semi-automatic algorithm that addressed the IMC segmentation in sequences of B-mode ultrasound images was proposed by Destrepes *et al.* [17]. Their algorithm relies on the assumption that the echogenicity of the region of interest that encompasses the IMC can be accurately modeled using a mixture of three Nakagami distributions and in their approach they estimated the parameters of these distributions using an expectation-maximization (EM) algorithm. Similar to the approach detailed in [16], the first stage of the algorithm proposed by Destrepes *et al.* [17] involves a user-driven process that is applied to select a set of points that are used to initialize the IMC interfaces in the first frame of the se-

quence. From this manual initialization, their algorithm searches for piecewise segments located 2 mm above and below the manually marked IMC points that maximize the posterior distributions using an exploration selection (ES) optimization algorithm. Once the process associated with the identification of the IMC is completed, the algorithm commences the tracking in the subsequent frames. In this regard, the IMC interfaces located in the previous frames are used as initial solutions in the current frame and the algorithm searches for piecewise segments within 1 mm toward the lumen and 1 mm toward the adventitia using the same approach that has been employed to identify the IMC in the first frame of the video sequence. Destrepes *et al.* [17] reported a mean distance error for data annotated by two experts as follows:  $0.21 \text{ mm} \pm 0.13$  for the LI interface and  $0.16 \text{ mm} \pm 0.07$  for the MA interface for Expert 1 and  $0.18 \text{ mm} \pm 0.11$  for the LI interface and  $0.15 \text{ mm} \pm 0.1$  for the MA interface for Expert 2 (see Table II).

By analyzing the algorithmic solutions and performance indicators associated with [16] and [17], we can observe several issues that illustrate the superiority of our algorithm. First, our method does not require any level of user intervention during the IMC segmentation or during the LI and MA tracking process. Second, the performance returned by our method with respect to the identification of the IMC in video ultrasound CCA data is superior to those offered by both state-of-the-art algorithms. The mean errors recorded by our method are as follows:  $0.06 \text{ mm} \pm 0.03$  for the LI interface and  $0.08 \text{ mm} \pm 0.04$  for the MA interface. In addition, the proposed method outperforms the approaches detailed in [16] and [17] with respect to the computational time. For the method detailed in [16], the reported computational time required to track the IMC in a video sequence that consists of 80 frames is 8.2 minutes (this translates into a processing time of 6.15 seconds per frame), whereas the computational overhead associated with the method proposed by Destrepes *et al.* [17] is 14 hours and 41 minutes to identify the IMC in 30 video sequences (the average computational time is 24 seconds per frame). The method detailed in our paper is faster, requiring a computational time between 1.0 and 2.5 s to process one frame.

At this point, we emphasize the predominantly supervised nature of the approaches listed in Table II. Following a detailed analysis of the published works on IMC segmentation listed in Table II, it is important to mention that they were built on the assumption that the adventitia is characterized by pixels defined by maximum intensity values. Consequently, this information was used to construct salient intensity profiles that were applied to localize the arterial layers in the ultrasound data. Two major drawbacks are worth mentioning: The first drawback is related to the fact that in ultrasound clinical data the adventitia is not always characterized by maximum intensity values and as a result these approaches will fail to return the expected results. The second drawback is given by the potential risk of confusing the carotid artery with the

TABLE II. SUMMARY PERFORMANCE OF IMC SEGMENTATION ALGORITHMS.

Algorithm	Year	Still/ video	Data set	Reported numerical results		
				Proposed method	Expert 1	Expert 2
Selzer <i>et al.</i> [16]	2001	Video	24 CCA sequences, (2 visits, 1 week apart)	Visit 1 IMT <sub>min</sub> 0.77 ± 0.16 IMT <sub>max</sub> 0.80 ± 0.17 (IMT <sub>mean</sub> ± σ) = 0.93 mm ± 0.25 CV% = 1.4	Visit 2 0.76 ± 0.16 0.80 ± 0.16	CV% 4.03 3.46
Wendelhag <i>et al.</i> [10]	1997	Still	50 images	(IMT <sub>mean</sub> ± σ) = 0.93 mm ± 0.25 CV% = 1.4		
Liang <i>et al.</i> [11]	2000	Still	50 patients	(IMT <sub>mean</sub> ± σ) = 0.93 mm ± 0.25 CV% = 2		(IMT <sub>mean</sub> ± σ) = 0.88 mm ± 0.25 (IMT <sub>mean</sub> ± σ) = 0.88 mm ± 0.25
Golemati <i>et al.</i> [22]	2007	Still	10 patients	IMT <sub>mean_systole</sub> = 0.55 mm ± 0.06 and IMT <sub>mean_diastole</sub> = 0.61 mm ± 0.05		
Gutierrez <i>et al.</i> [23]	2002	Still	30 images	(IMT <sub>mean</sub> ± σ) = 0.72 mm ± 0.14 CV% = 6.16		(IMT <sub>mean</sub> ± σ) = 0.63 mm ± 0.12
Ilea and Whelan [24]	2009	Still	49 images	LI <sub>border_displacement_error</sub> (proposed method, ground truth) = 0.079 mm MA <sub>border_displacement_error</sub> (proposed method, ground truth) = 0.082 mm		
Destrempes <i>et al.</i> [17]	2009	Video	30 sequences, 15 CCA + 15 ICA	For CCA only (15 patients): LI <sub>mean_distance_error</sub> (proposed method, ground truth <sub>Expert1</sub> ) = 0.21 mm ± 0.13 MA <sub>mean_distance_error</sub> (proposed method, ground truth <sub>Expert1</sub> ) = 0.16 mm ± 0.07 LI <sub>mean_distance_error</sub> (proposed method, ground truth <sub>Expert2</sub> ) = 0.18 mm ± 0.11 MA <sub>mean_distance_error</sub> (proposed method, ground truth <sub>Expert2</sub> ) = 0.15 mm ± 0.11 IMT <sub>mean</sub> = 0.68 ± 0.12 mm (best result)		IMT <sub>mean_visit1</sub> = 0.67 mm ± 0.16 IMT <sub>mean_visit2</sub> = 0.67 mm ± 0.16
Loizou <i>et al.</i> [25]	2007	Still	- 100 images - 2 visits (12 mo apart)			IMT <sub>mean_visit1</sub> = 0.65 mm ± 0.18 IMT <sub>mean_visit2</sub> = 0.55 mm ± 0.11
Cheng <i>et al.</i> [26]	2002	Still	32 images	LI <sub>mean_square_error</sub> (proposed method, ground truth) = 0.65 and MA <sub>mean_square_error</sub> (proposed method, ground truth) = 0.40		
Rocha <i>et al.</i> [28]	2010	Still	47 images from 24 patients	CV <sub>IMTmean</sub> (proposed method, ground truth <sub>Expert1</sub> ) = 7.7% CV <sub>IMTmean</sub> (proposed method, ground truth <sub>Expert2</sub> ) = 8.3% CV <sub>IMTmean</sub> (proposed method, ground truth <sub>Expert2</sub> ) = 8.4% (after 1 year)		
Delsanto <i>et al.</i> [29]	2007	Still	120 images, 31 patients	LI <sub>mean_segmentation_error</sub> = 0.95 ± 1.04 pixels MA <sub>mean_segmentation_error</sub> = 0.77 ± 0.80 pixels		
Molinari <i>et al.</i> [30]	2010	Still	182 images (in 18 CCA misidentified)	IMT <sub>mean</sub> = 0.75 mm ± 0.39		IMT <sub>mean</sub> = 0.92 mm ± 0.30
Molinari <i>et al.</i> [31]	2011	Still	365 images	IMT <sub>mean_absolute_error</sub> = 0.054 mm ± 0.035 IMT <sub>mean</sub> = 0.91 mm ± 0.44		IMT <sub>mean</sub> = 0.95 mm ± 0.39
Loizou <i>et al.</i> [32]	2009	Still	100 images	LI <sub>error</sub> = 0.081 mm ± 0.099 and MA <sub>error</sub> = 0.082 mm ± 0.197 IMT <sub>mean</sub> = 0.67 mm ± 0.12		IMT <sub>mean</sub> = 0.71 mm ± 0.17 IMT <sub>mean</sub> = 0.72 mm ± 0.17 (6 mo later)
Proposed method	2012	Video	40 data sets, 772 frames	LI <sub>mean_error</sub> (proposed method, ground truth) = 0.06 mm ± 0.03 and MA <sub>mean_error</sub> (proposed method, ground truth) = 0.08 mm ± 0.04 IMT <sub>mean</sub> = 0.60 mm ± 0.10		IMT <sub>mean</sub> = 0.60 mm ± 0.11

The numerical results are those reported by the authors in the original papers.  
CCA = common carotid artery; CV = coefficient of variation; IMT = intima media thickness; ICA = internal carotid artery.



jugular vein and in this case the region of interest (ROI) will be erroneously selected. To address these problems, in this paper, we introduced an algorithm that is able to identify the IMC interfaces in an unsupervised manner, where the proposed solution is not adversely influenced by the changes in morphological properties of the carotid that are patient-characteristic. Although the user intervention proved opportune because it reduced, to a large extent, the errors in the IMC ROI detection, there is little doubt that this solution is far from optimal when applied to large ultrasound image sequences. To remove the reliance on the user interaction (which is a characteristic of the majority of algorithms listed in Table II), in our implementation, we have maximized the use of the anatomic knowledge in the process required to locate the far wall of the carotid artery in ultrasound data. The precise identification of the far wall interface opened the opportunity to develop an efficient model-based IMC segmentation strategy that primarily consists of a multi-resolution edge reconstruction process.

The second important point we want to make in this discussion relates to the strategies employed for the segmentation of the IMC in still and video CCA data. Because of the large spectrum of practical advantages that are achieved by enforcing spatial continuity constraints in the process of IMC segmentation, the snake-based approaches were popular among many researchers. Despite their initial enthusiasm, many studies [23], [25]–[27], [29], [49] emphasized several practical and theoretical limitations associated with the snake-based approaches when applied to the IMC segmentation. The most obvious ones are related to the complexity of the contour initialization process and the poor contrast between the MA interface and the surrounding arterial tissues. The latter problem proved more challenging and to alleviate the occurrence of errors during the energy minimization process, researchers have adopted various custom-designed solutions to implement advection forces ([25], [26]) that prevent the MA and LI interfaces from settling on incorrect arterial structures. Dynamic programming algorithms were proposed as a computationally efficient alternative to the standard heuristic contour search methods, and because of their intrinsic properties, they proved an attractive approach for IMC segmentation [11], [28], [50]. However, these approaches have several limitations, including their inability to capture deep concavities and sharp saliencies [11], and their rigid architecture is not particularly well suited to address the problems generated by the inconsistent LI and MA gradient profiles that are often encountered in clinical CCA ultrasound data. All issues associated with the inconsistencies of the LI and MA interfaces are substantially exacerbated when the algorithms are applied to video (2-D + time) CCA data and this motivates the development of more targeted strategies, such as that detailed in this paper.

The last issue that we would like to address in this discussion relates to the quantitative evaluation of the pro-

posed method that was detailed in Section II. As indicated in Section III, the performance in terms of the identification of the LI and MA interfaces proved very encouraging, and this study allowed the identification of several clinical needs that can be addressed by the proposed IMC segmentation and tracking algorithm. By analyzing the mean IMT values obtained for each video sequence used in our experimental study, we found that the patients' demographics were mirrored in the numerical results. Because the study was conducted on healthy and asymptomatic patients (some patients had clinical conditions that could put them at risk of early cardiovascular diseases, as discussed in Section II-A.), the obtained IMT mean value was low ( $0.6 \text{ mm} \pm 0.1$ ). Three patients were identified to be at a higher risk of developing atherosclerosis, having a high mean IMT, and this was in accordance to their clinical condition. For patients D5 (48-year-old smoker) and D18 (37-year-old male with high cholesterol levels), the automatically measured  $\text{IMT}_{\text{mean}}$  was 0.81 mm, and for the patient D21 (31-year-old female with high cholesterol levels) the  $\text{IMT}_{\text{mean}}$  was 0.86 mm.

Another interesting issue emerging from our study is associated with the box plots depicted in Fig. 11 that display the coefficient of variation (CV %) of the  $\text{IMT}_{\text{mean}}$  values recorded for automatic and manual IMT measurements. The experimental results show that in 39 out of 40 datasets, the CV is higher for manually annotated data, which emphasizes that the manual measurements are more dispersed within the same dataset when compared to the automatic segmentation results. This finding raises an important issue that illustrates the potential bias that can be inserted during the manual annotation process and motivates the use of CAD solutions as a second reader. Fig. 14 brings to surface an additional research topic that received limited attention in previous studies—i.e., the variation of the IMT from the end diastolic phase to the peak systolic phase of the cardiac cycle. The change in the IMT over the cardiac cycle has the potential to complement the results that relate to the elastic properties of the arterial wall, because these measurements may have clinical use in the evaluation of the arterial stiffness [46]. The reader can refer to [16], [46], and [52]–[55], where additional studies were conducted to evaluate the relation between the change in the IMT and the arterial stiffness. Among these, the clinical study by Meinders *et al.* [46] is the most relevant, in which the authors evaluated in detail the dynamic behavior of the IMC to assess the local structural and mechanical changes in the arterial walls in the presence of arterial lesions. We conclude that the changes in the IMT over the cardiac cycle may have pathophysiological relevance, because the thickening of the intimal and medial layers is caused by muscle hypertrophy, inflammatory cell infiltration, deposition of lipids, and/or calcification. All of these factors are likely to induce different deformation patterns, whose identification may allow a more accurate prediction of future cardiovascular events.

## V. CONCLUDING REMARKS AND FUTURE WORK

A distinct characteristic of the majority of the published works that addressed the IMC segmentation is the substantial level of supervision that is required to compensate for the errors that are generated by the challenging imaging conditions that are present in the CCA video ultrasound data. The major objective of this paper was to introduce a new automatic methodology for the segmentation and tracking of the two IMC interfaces in longitudinal carotid B-mode video ultrasound sequences that is able to identify in an unsupervised manner the IMT changes and the LI and MA displacements during the cardiac cycle. The proposed algorithm entails a multi-stage ultrasound data analysis. In the first stage, an unsupervised method for the segmentation of the IMC in the first frame of the sequence was proposed. A particular novelty associated with the proposed IMC segmentation algorithm is the application of a suite of geometric and anatomic constraints to ensure that the IMC interfaces do not converge on erroneous vascular structures. The next phase of the algorithm involves the application of a novel tracking procedure that is referred to as ANC, which is employed for the detection of the MA and LI interfaces in the subsequent frames of the 2-D + time video sequence. An important advantage of the proposed ANC algorithm is its ability to accommodate the inconsistencies in the structure of the IMC in consecutive images that encompass the cardiac cycle. The quantitative evaluation that was used to assess the performance of the developed algorithm indicates a good correlation between the results returned by the proposed IMC segmentation and tracking algorithm and those calculated from the manually annotated ground truth data. Our experimental study revealed several interesting issues in relation to the assessment of the IMT in video ultrasound data. First, the recorded IMT results indicate that the proposed automatic technique returns consistent results and its performance recommends its use in clinical studies as a second reader. Second, the evaluation of the IMT over the cardiac cycle allows the extraction of additional indicators that can be used in the assessment of the arterial dynamics, which may allow a more accurate prediction of future cardiovascular events. Currently, the proposed algorithm is being evaluated in clinical trials in Beaumont Hospital, Dublin, Ireland. This research is ongoing and the future clinical studies will focus on the evaluation of patients that are affected by advanced cardiovascular conditions, such as focal thickening and arterial plaques.

## REFERENCES

- [1] I. M. van der Meer, M. L. Bots, A. Hofman, A. I. del Sol, D. A. van der Kuip, and J. C. Witteman, "Predictive value of noninvasive measures of atherosclerosis for incident myocardial infarction: The Rotterdam study," *Circulation*, vol. 109, no. 9, pp. 1089–1094, 2004.
- [2] R. Ross, "The pathogenesis of atherosclerosis: A perspective for the 1990s," *Nature*, vol. 362, no. 6423, pp. 801–809, Apr. 1993.
- [3] F. Orzan, M. Anselmino, and M. Camillo, "Cardiovascular risk in subjects with carotid pathologies," in *Atherosclerosis Disease Management*, J. S. Suri, C. Kathuria, and F. Molinari, Eds., Berlin, Germany: Springer Science and Business Media, 2011, pp. 37–51.
- [4] F. Molinari and J. S. Suri, "Automated measurement of carotid artery intima-media thickness," in *Ultrasound and Carotid Bifurcation Atherosclerosis*, part 3, A. Nicolaides, K. W. Beach, E. Kyriacou, and C. S. Pattichis, Eds., London, UK: Springer-Verlag, 2012, pp. 177–192.
- [5] M. Cinthio, A. R. Ahlgren, T. Jansson, A. Eriksson, H. W. Persson, and K. Lindstrom, "Evaluation of an ultrasonic echo-tracking method for measurements of arterial wall movements in two dimensions," *IEEE Trans. Ultrason. Ferroelectr. Freq. Control*, vol. 52, no. 8, pp. 1300–1311, Aug. 2005.
- [6] S. Golemati, A. Sassano, M. J. Lever, A. A. Bharath, D. T. Dhanjil, and A. N. Nicolaides, "Carotid artery wall motion estimated from B-mode ultrasound using region tracking and block matching," *Ultrasound Med. Biol.*, vol. 29, no. 3, pp. 387–399, Mar. 2003.
- [7] M. A. Lubinski, S. Y. Emelianov, and M. O'Donnell, "Speckle tracking methods for ultrasonic elasticity imaging using short-time correlation," *IEEE Trans. Ultrason. Ferroelectr. Freq. Control*, vol. 46, no. 1, pp. 82–96, Jan. 1999.
- [8] E. Bianchini, C. Giannarelli, F. Faita, K. Raimo, V. Gemignani, L. Ghiadoni, and M. Demi, "The assessment of local arterial stiffness from ultrasound images," in *Proc. 34th Annu. Int. Computers in Cardiology Conf.*, 2007, pp. 761–764.
- [9] I. Wendelhag, T. Gustavsson, M. Suurkula, G. Berglund, and J. Wikstrand, "Ultrasound measurement of wall thickness in the carotid artery: Fundamental principles and description of a computerized analysing system," *Clin. Physiol.*, vol. 11, no. 6, pp. 565–577, 1991.
- [10] I. Wendelhag, Q. Liang, T. Gustavsson, and J. Wikstrand, "A new automated computerized analyzing system simplifies readings and reduces the variability in ultrasound measurement of intima-media thickness," *Stroke*, vol. 28, no. 11, pp. 2195–2200, 1997.
- [11] Q. Liang, I. Wendelhag, J. Wikstrand, and T. Gustavsson, "A multiscale dynamic programming procedure for boundary detection in ultrasonic artery images," *IEEE Trans. Med. Imaging*, vol. 19, no. 2, pp. 127–142, Feb. 2000.
- [12] J. F. Polak, L. C. Funk, and D. H. O'Leary, "Inter-reader differences in common carotid artery intima-media thickness: Implications for cardiovascular risk assessment and vascular age determination," *J. Ultrasound Med.*, vol. 30, no. 7, pp. 915–920, 2011.
- [13] J. F. Polak, M. J. Pencina, D. Herrington, and D. H. O'Leary, "Associations of edge-detected and manual-traced common carotid intima-media thickness measurements with Framingham risk factors: The multi-ethnic study of atherosclerosis," *Stroke*, vol. 42, no. 7, pp. 1912–1916, 2011.
- [14] J. F. Polak, M. J. Pencina, A. Meisner, K. M. Pencina, L. S. Brown, P. A. Wolf, and R. B. D'Agostino Sr., "Associations of carotid artery intima-media thickness (IMT) with risk factors and prevalent cardiovascular disease: Comparison of mean common carotid artery IMT with maximum internal carotid artery IMT," *J. Ultrasound Med.*, vol. 29, no. 12, pp. 1759–1768, Dec. 2010.
- [15] P. J. Touboul, E. Vicaut, J. Labreuche, J. P. Belliard, S. Cohen, S. Kownator, and I. Pithois-Merli, "Design, baseline characteristics and carotid intima-media thickness reproducibility in the PARC study," *Cerebrovasc. Dis.*, vol. 19, no. 1, pp. 57–63, 2005.
- [16] R. H. Selzer, W. J. Mack, P. L. Lee, H. Kwong-Fu, and H. N. Hodis, "Improved carotid elasticity and intima-media thickness measurements from computer analysis of sequential ultrasound frames," *Atherosclerosis*, vol. 154, no. 1, pp. 185–193, 2001.
- [17] F. Destrempe, J. Meunier, M. F. Giroux, G. Soulez, and G. Cloutier, "Segmentation in ultrasonic B-mode images of healthy carotid arteries using mixtures of Nakagami distributions and stochastic optimization," *IEEE Trans. Med. Imaging*, vol. 28, no. 2, pp. 215–229, Feb. 2009.
- [18] R. H. Selzer, H. N. Hodis, H. Kwong Fu, W. J. Mack, P. L. Lee, C. R. Liu, and C. H. Liu, "Evaluation of computerized edge tracking for quantifying intima-media thickness of the common carotid artery from B-mode ultrasound images," *Atherosclerosis*, vol. 111, pp. 1–11, 1994.
- [19] J. H. Dwyer, P. Sun, H. Kwong-Fu, K. M. Dwyer, and R. H. Selzer, "Automated intima-media thickness: The Los Angeles atherosclerosis study," *Ultrasound Med. Biol.*, vol. 24, no. 7, pp. 981–987, Sep. 1998.

- [20] P. Liguori, A. Paolillo, and A. Pietrosanto, "An automatic measurement system for the evaluation of carotid intima-media thickness," *IEEE Trans. Instrum. Meas.*, vol. 50, no. 6, pp. 1684–1691, Dec. 2001.
- [21] F. Faita, V. Gemignani, E. Bianchini, C. Giannarelli, and M. Demi, "Real-time measurement system for the evaluation of the intima media thickness with a new edge detector," in *Proc. 28th Annu. Int. Conf. IEEE Eng. Med. Biol. Soc.*, 2006, pp. 715–718.
- [22] S. Golemati, J. Stoitsis, E. G. Sifakis, T. Balkizas, and K. S. Nikita, "Using the Hough transform to segment ultrasound images of longitudinal and transverse sections of the carotid artery," *Ultrasound Med. Biol.*, vol. 33, no. 12, pp. 1918–1932, Dec. 2007.
- [23] M. A. Gutierrez, P. E. Pilon, S. G. Lage, L. Kopel, R. T. Carvalho, and S. S. Furuie, "Automatic measurement of carotid diameter and wall thickness in ultrasound images," *Comput. Cardiol.*, vol. 29, pp. 359–362, 2002.
- [24] D. E. Ilea, P. F. Whelan, C. Brown, and A. Stanton, "An automatic 2D CAD algorithm for the segmentation of the IMT in ultrasound carotid artery images," in *Proc. 31st Annu. Int. Conf. IEEE Eng. Med. Biol. Soc.: Engineering the Future of Biomedicine*, 2009, pp. 515–519.
- [25] C. P. Loizou, C. S. Pattichis, M. Pantziaris, T. Tyllis, and A. Nicolaides, "Snakes based segmentation of the common carotid artery intima media," *Med. Biol. Eng. Comput.*, vol. 45, no. 1, pp. 35–49, Jan. 2007.
- [26] D. C. Cheng, A. Schmidt-Trucksäss, K. S. Cheng, and H. Burkhardt, "Using snakes to detect the intimal and adventitial layers of the common carotid artery wall in sonographic images," *Comput. Methods Programs Biomed.*, vol. 67, no. 1, pp. 27–37, Jan. 2002.
- [27] R. C. Chan, J. Kaufhold, L. C. Hemphill, R. S. Lees, and W. C. Karl, "Anisotropic edge-preserving smoothing in carotid B-mode ultrasound for improved segmentation and intima-media thickness (IMT) measurement," *Comput. Cardiol.*, vol. 27, pp. 37–40, 2000.
- [28] R. Rocha, A. Campilho, J. Silva, E. Azevedo, and R. Santos, "Segmentation of the carotid intima-media region in B-mode ultrasound images," *Image Vis. Comput.*, vol. 28, no. 4, pp. 614–625, Apr. 2010.
- [29] S. Delsanto, F. Molinari, P. Giustetto, W. Liboni, S. Badalamenti, and J. S. Suri, "Characterization of a completely user-independent algorithm for carotid artery segmentation in 2-D ultrasound images," *IEEE Trans. Instrum. Meas.*, vol. 56, no. 4, pp. 1265–1274, Aug. 2007.
- [30] F. Molinari, G. Zeng, and J. S. Suri, "Intima-media thickness: Setting a standard for a completely automated method of ultrasound measurement," *IEEE Trans. Ultrason. Ferroelectr. Freq. Control*, vol. 57, no. 5, pp. 1112–1124, 2010.
- [31] F. Molinari, C. Pattichis, G. Zeng, L. Saba, U. Acharya, R. Sanfilippo, A. Nicolaides, and J. Suri, "Completely automated multi-resolution edge snapper (CAMES)—A new technique for an accurate carotid ultrasound IMT measurement: Clinical validation and benchmarking on a multi-institutional database," *IEEE Trans. Image Process.*, vol. 21, no. 3, pp. 1211–1222, Sep. 2012.
- [32] C. P. Loizou, C. S. Pattichis, A. N. Nicolaides, and M. Pantziaris, "Manual and automated media and intima thickness measurements of the common carotid artery," *IEEE Trans. Ultrason. Ferroelectr. Freq. Control*, vol. 56, no. 5, pp. 983–994, May 2009.
- [33] N. Otsu, "A threshold selection method from grey-level histograms," *IEEE Trans. Syst. Man Cybern.*, vol. 9, no. 1, pp. 62–66, Jan. 1979.
- [34] C. P. Loizou, C. S. Pattichis, C. I. Christodoulou, R. S. H. Istepanian, M. Pantziaris, and A. Nicolaides, "Comparative evaluation of despeckle filtering in ultrasound imaging of the carotid artery," *IEEE Trans. Ultrason. Ferroelectr. Freq. Control*, vol. 52, no. 10, pp. 1653–1669, Oct. 2005.
- [35] J. A. Noble and D. Boukerroui, "Ultrasound image segmentation: A survey," *IEEE Trans. Med. Imaging*, vol. 25, no. 8, pp. 987–1010, Aug. 2006.
- [36] V. Dutt and J. F. Greenleaf, "Adaptive speckle reduction filter for log-compressed B-scan images," *IEEE Trans. Med. Imaging*, vol. 15, no. 6, pp. 802–813, 1996.
- [37] R. F. Wagner, S. W. Smith, J. M. Sandrik, and H. Lopez, "Statistics of speckle in ultrasound B-scans," *IEEE Trans. Sonics Ultrason.*, vol. 30, no. 3, pp. 156–163, 1983.
- [38] C. B. Burckhardt, "Speckle in ultrasound B-mode scans," *IEEE Trans. Sonics Ultrason.*, vol. SU-25, no. 1, pp. 1–6, 1978.
- [39] J. Astola, P. Haavisto, and Y. Nuevo, "Vector median filters," *Proc. IEEE*, vol. 79, pp. 678–689, 1990.
- [40] J. Canny, "A computational approach to edge detection," *IEEE Trans. Pattern Anal. Mach. Intell.*, vol. 8, no. 6, pp. 679–698, 1986.
- [41] J. F. Kenney and E. S. Keeping, "Linear regression and correlation," in *Mathematics of Statistics*, pt. 1, 3rd ed. Princeton, NJ: Van Nostrand, 1962, ch. 15, pp. 252–285.
- [42] B. H. Friemel, L. N. Bohs, and G. E. Trahey, "Relative performance of two-dimensional speckle-tracking techniques: Normalized correlation, non-normalized correlation and sum-absolute-difference," in *Proc. IEEE Ultrason. Symp.*, 1995, vol. 2, pp. 1481–1484.
- [43] J. M. Bland and D. G. Altman, "Statistical methods for assessing agreement between two methods of clinical measurement," *Lancet*, vol. 1, no. 8476, pp. 307–310, 1986.
- [44] D. G. Altman and J. M. Bland, "Measurement in medicine: The analysis of measurement comparison studies," *Statistician*, vol. 32, no. 3, pp. 307–317, 1983.
- [45] F. Wilcoxon, "Individual comparisons by ranking methods," *Biom. Bull.*, vol. 1, no. 6, pp. 80–83, 1945.
- [46] J. M. Meinders, L. Kornet, and A. P. Hoeks, "Assessment of spatial inhomogeneities in intima media thickness along an arterial segment using its dynamic behavior," *Am. J. Physiol. Heart Circ. Physiol.*, vol. 285, no. 1, pp. H384–H391, 2003.
- [47] F. Faita, V. Gemignani, E. Bianchini, C. Giannarelli, L. Ghiadoni, and M. Demi, "Real-time measurement system for evaluation of the carotid intima-media thickness with a robust edge operator," *J. Ultrasound Med.*, vol. 27, no. 9, pp. 1353–1361, 2008.
- [48] D. E. Ilea, P. F. Whelan, C. Brown, and A. Stanton, "Automatic detection and measurement of the IMT in longitudinal sections of ultrasound images of the CCA," in *European Congress of Radiology (ECR)*, 2010, art. no. SS 1205, B-522.
- [49] M. C. Bastida-Jumilla, J. Morales-Sánchez, R. Verdú-Monedero, J. Larrey-Ruiz, and J. L. Sancho-Gómez, "Detection of the intima and media walls of the carotid artery with geodesic active contours," in *Proc. 17th Int. Conf. Image Processing*, 2010, pp. 2213–2216.
- [50] D. C. Cheng and X. Jiang, "Detections of arterial wall in sonographic artery images using dual dynamic programming," *IEEE Trans. Inf. Technol. Biomed.*, vol. 12, no. 6, pp. 792–799, 2008.
- [51] F. Molinari, G. Zeng, and J. S. Suri, "A state of the art review on intima-media thickness (IMT) measurement and wall segmentation techniques for carotid ultrasound," *Comput. Methods Programs Biomed.*, vol. 100, no. 3, pp. 201–221, Dec. 2010.
- [52] Y. F. Cheung, S. J. Wong, and M. H. K. Ho, "Relationship between carotid intima-media thickness and arterial stiffness in children after Kawasaki disease," *Arch. Dis. Child.*, vol. 92, no. 1, pp. 43–47, 2007.
- [53] D. M. Herrington, W. V. Brown, L. Mosca, W. Davis, B. Eggleston, W. G. Hundley, and J. Raines, "Relationship between arterial stiffness and subclinical aortic atherosclerosis," *Circulation*, vol. 110, no. 4, pp. 432–437, 2004.
- [54] K. S. Cheng, D. P. Mikhailidis, G. Hamilton, and A. M. Seifalian, "A review of the carotid and femoral intima-media thickness as an indicator of the presence of peripheral vascular disease and cardiovascular risk factors," *Cardiovasc. Res.*, vol. 54, no. 3, pp. 528–538, 2002.
- [55] A. D. Augst, B. Ariff, S. A. McG. Thom, X. Y. Xu, and A. D. Hughes, "Analysis of complex flow and the relationship between blood pressure, wall shear stress, and intima-media thickness in the human carotid artery," *Am. J. Physiol. Heart Circ. Physiol.*, vol. 293, no. 2, pp. H1031–H1037, 2007.



**Dana E. Ilea** received her B.Eng. degree (Hons) in electronic engineering and computer science from Transilvania University, Brasov, Romania, in 2005 and her Ph.D. degree in computer vision from Dublin City University, Dublin, Ireland, in 2008. Since 2008, she has held the position of Post-Doctoral Researcher within the Centre for Image Processing and Analysis (CIPA), Dublin City University. Her main research interests are in the areas of image processing, texture and color analysis, and medical imaging.



**Caoimhe Duffy** received her M.B., B.Ch., B.A.O., B.Med.Sci. (NUI, RCSI), LRCP&SI degrees from the Royal College of Surgeons in Ireland in 2011. She worked as an intern doctor at Beaumont Hospital, Dublin, and she currently holds the position of Senior House Officer in the National Rehabilitation Centre, Dun Laoghaire, Ireland.



**Liam N. Kavanagh** received his M.B., B.Ch., B.A.O. (Hons) degree from the Royal College of Surgeons in Ireland (RCSI) in 2006 and completed his General Professional Training in medicine at Beaumont Hospital, Dublin, in 2009. From July 2009 to June 2011, he worked as a clinical research fellow for the Department of Molecular and Cellular Therapeutics at the RCSI. He is a Member of the Royal College of Physicians in the United Kingdom and currently works as a Specialist Registrar in Radiology at Beaumont Hospital in Dublin.



**Alice Stanton** graduated from University College Dublin with an honors degree in medicine in 1984, and has since obtained a first-class honors degree in physiology from University College Dublin, a postgraduate diploma in statistics with distinction from Trinity College Dublin, and a Ph.D. in pharmacology from University College Dublin. Clinical training in general internal medicine and clinical pharmacology was obtained at St. Vincent's University Hospital Dublin, St. Lawrence's Hospital Dublin, Mater Misericordiae Hospital

Dublin, Hammersmith Hospital London, Academisch Ziekenhuis Utrecht, Beaumont Hospital Dublin, St. Mary's Hospital, and Imperial College,

London. She became a Fellow of the Royal Colleges of Physicians in Ireland (RCSI) in 2003. She is currently an Associate Professor in molecular and cellular therapeutics at RCSI. She holds specialist cardiovascular medicine clinics at Beaumont Hospital and at the National Maternity Hospital, Dublin. Her particular research interests include hypertension, noninvasive measurement and imaging of vascular structure and function, cardiovascular genetics, and personalized medicine. She is currently a member of the International Society of Hypertension, the European Society of Hypertension, the European Council for Cardiovascular Research, the British Hypertension Society, and the Irish Heart Foundation's Council on High Blood Pressure. She has authored more than 80 peer-reviewed, published papers, 4 book chapters, 4 editorials, and 10 reviews. Over the last 15 years, she has received both fellowships and project grants from the European Society of Cardiology, the British Heart Foundation, the Medical Research Council (UK), the Engineering Physical Science Research Council (UK), the Health Research Board (Ireland), Charitable Infirmity Charitable Trust (Ireland), Enterprise Ireland, the Higher Education Authority (Ireland), and the European Commission Seventh Framework Programme.



**Paul F. Whelan** received his B.Eng. (Hons) degree from NIHED, his M.Eng. degree from the University of Limerick, and his Ph.D. degree in computer vision from Cardiff University (UK). During the period from 1985 to 1990, he was employed by Industrial and Scientific Imaging Ltd. and later Westinghouse (WESL), where he was involved in the research and development of high-speed computer vision systems. He was appointed to the School of Electronic Engineering, Dublin City University (DCU) in 1990 and is currently

Professor of Computer Vision (Personal Chair). Prof. Whelan set up the Vision Systems Laboratory and its associated Vision Systems Group in 1990 and the Centre for Image Processing and Analysis in 2006 and currently serves as its director. He also serves on the steering committee of the RINCE institute (an Irish national research institute focused on innovation in engineering technologies) and is a PI in the National Biophotonics & Imaging Platform Ireland (NBIPi).

As well as publishing more than 150 peer-reviewed papers, Prof. Whelan has co-authored 2 monographs and co-edited 3 books. His research interests include image segmentation, and its associated quantitative analysis (specifically, mathematical morphology and color-texture analysis) with applications in computer/machine vision and medical imaging (specifically, computer-aided detection and diagnosis focusing on translational research). He is a Senior Member of the IEEE, a Chartered Engineer, a member of the International Association for Pattern Recognition (IAPR), and a Fellow of the Institution of Engineering and Technology (IET). He served on the IEE Irish centre committee (1999–2002) and as the national representative and member of the governing board (1998–2007) of IAPR, a member of the International Federation of Classification Societies (IFCS) council and the inaugural President (1998–2007) of the Irish Pattern Recognition and Classification Society.